A CAPACITIVE MONITORING SYSTEM FOR STEREOTACTIC
RADIOSURGERY: DETECTOR DESIGN

by

Ethan Antonio Avila Ruiz

Submitted in partial fulfilment of the requirements
for the degree of Master of Science

at

Dalhousie University
Halifax, Nova Scotia
August 2017

TABLE OF CONTENTS

LIST OF TABLES

LIST OF FIGURES

vii

ABSTRACT

In this thesis, a novel capacitive detector allowing near real-time monitoring of the cranium during stereotactic radiosurgery (SRS) is developed and evaluated. The variation in sensitivity (signal change per mm) was investigated with regard to: (i) the material of the capacitive plate, (ii) the shape of the plate and (iii) the area and thickness of the plate. This was carried out using a parallel plate setup. Several designs were investigated in a limited volunteer study with the detector proximal to the cranium. The proposed capacitive detectors demonstrated acceptable sensitivity for guidance of SRS, up to 41 %/mm, and could be read out at 200 Hz with coefficient of variation of 0.14 %. The detectors investigated here provide a range of 15 mm and are able to detect sub-millimetre patient motions. The detectors are sensitive to the position of the cranium inside a patient's thermoplastic mask, but offer the advantage of being comparatively insensitive to the mask itself.

LIST OF ABBREVIATIONS USED

3D-CRT	Three-Dimensional Conformal Radiation Therapy
ADC	Analog-to-Digital Converter
AWG	American Wire Gauge
CT	Computed Tomography
CBCT	Cone Beam Computed Tomography
DC	Direct Current
GUI	Graphical User Interface
I2C	Inter-Integrated Circuit
IMRT	Intensity modulated radiation therapy
LINAC	Linear Accelerator
MeV	Megaelectron-volt
MLC	Multi-leaf Collimator
MU	Monitor Units
MV	Megavoltage
NI	National Instruments
SAD	Source-to-Axis Distance
SBRT	Stereotactic Body Radiation Therapy
SNR	Signal-to-Noise ratio
SRS	Stereotactic radiosurgery
SSD	Source-to-Surface Distance
UL	Underwriters Laboratory
VMAT	Volumetric Modulated Arc Therapy
Z	Atomic Number

ACKNOWLEDGEMENTS

First, I would like to thank my supervisor Dr. James Robar for his continuous support throughout this project. Without your guidance and encouragement this research would not have been what it is today. Even when times were tough, your general support was enough to help me keep going and give my best every step of the way. Thank you for sharing your knowledge with me and always being there to answer all my questions, no matter how small they were.

I would also like to Dr. Krista Chytyk-Praznik and Dr. Alasdair Syme, my committee members, for providing a different point of view to the project and constructive criticism throughout this past year. I appreciate all of your comments and suggestion and hope to keep learning from you as I move on to the next step in my academic career.

I would like to thank my friends and colleagues in the Medical Physics program for being a constant source of encouragement as well as comradeship. Without you these past two years would not have been the same.

Finally, I would like to thank my family for their support over the past two years. Thank you for always being supportive and caring. Thank you for never giving up on me, even when we are thousands of miles apart.

CHAPTER 1   INTRODUCTION

1.1 PREFACE

In Canada 1 in 2 Canadians will develop cancer in their lifetime. An estimated 80, 800 Canadians will die of the disease in 2017 (1). Cancer incidence has seen an overall increase in recent years. For some cancers this may relate to improved means of detection while others may be related to an increase in risk factors. In contrast, the mortality rate of cancer has decreased steadily over the past several decades (1). This decrease in mortality rates is often attributed to an improved understanding of the disease and an improvement in both detection and treatment. According to the National Institutes of Health and the National Center for Health Statistics, in 2016, cancer was the disease with most support funds for research. In 2017 this number is expected to increase by 8 % (2).

The techniques currently used for treatment of cancer, such as surgery, chemotherapy, immunotherapy and radiation therapy are constantly being updated to improve efficiency of treatments. Chemotherapy, a systemic treatment used to focus uptake of drugs primarily in cancer cells, has recently started using nanoparticles to enhance delivery strategies to encapsulate various drugs simultaneously (3). Immunotherapy is a treatment that increases the body's immune response to stop and destroy cancer cells. Radiation therapy is a local treatment therapy that can be internal such as the case with brachytherapy or external therapy which involves the delivery of radiation from an external source to a targeted site in the patient.

1

External radiation therapy is commonly delivered using medical linear accelerators (linacs) which accelerate electrons to collide into a target with a high atomic number (Z) and produce high energy photons due to the physical process known as bremsstrahlung. Most of the advances in external radiation therapy are made in minimizing the effect of radiation in healthy tissues and increasing the tumor control probability. The therapeutic ratio denotes the relationship between the probability of tumor control and the likelihood of normal tissue damage. This is achieved by improving delivery of current treatments and minimizing the variability in patient alignment.

The treatment type to be used in the management of a patient's disease depends on various considerations including but not limited to the affected sites, patient history and extent of the disease. The effective treatment of cancer cells involves not only targeting the affected cells but also minimizing the damage to healthy tissue.

1.2 EXTERNAL-BEAM RADIATION THERAPY

1.2.1 History

External beam radiation therapy has a long history and has evolved continually for over 120 years. X-rays were discovered in 1895 by German physicist Wilhelm Röntgen and were first used for diagnostic imaging. A month after this discovery Léopold Freund and Eduard Schiff suggested that X-rays could be used in the treatment of diseases (4). A year after the discovery of X-rays, in Chicago, Emil Grubbe first used X-rays as treatment of the cancer diagnosis of a woman (5). The use of X-rays as treatment for cancer increased throughout the following years. This is considered to be the birth of radiation therapy.

Given the early adoption of X-rays in treatment there was little information as to the long-term effects of radiation. This led to a loss in faith in the effectiveness of X-rays for several years since there were reported cases were conditions were worsened after treatment (4).

Radiation therapy evolved with many refinements throughout the years. The introduction of multiple smaller doses in treatment over an extended period of time, or fractionation, is one such example. Many of the early advances came about as a result of a better understanding of the process through which radiation affects cells. The use of a fractionated regime as presented by Henri Coutard increased the effectiveness of treatment and reduced the side effects compared to those without fractionation (6). Furthermore, in 1934 Coutard developed the concept of a fractionated treatment regime that remains the basis for current radiation therapy (7). During the early stages of radiotherapy, due to technological limitations, most of the photon beams operated in the 200-500 kV energy range. These energies were useful to treat shallow tumors but for any tumors beyond 4-6 mm inside the body these energies were not sufficient. It wasn't until after the development of the Cobalt-60 unit in 1951 by Harold Johns, that high energy radiotherapy treatments (1.25 MeV) became widespread (8).

After the development of the Cobalt-60 unit more advances were made to increase the photon beam energies and thus increase the penetrating capability of the photon beam. In London, in 1953, the first 8 MV medical linear accelerator (linac) was used to treat a patient (9). Soon after in 1956, a 6 MV linac was used in the United States to treat a 2 year old boy with a retinoblastoma (10).

There is a wide variety of treatments available that make use of the technologies available using external-beam radiation therapy. Some of these treatments come from a better understanding of the physics of x-rays and the biology of the human body.

1.2.2 Ionizing Radiation

External-beam radiotherapy uses ionizing radiation to kill cancer cells and avoid further proliferation. Radiation beams traverse normal tissues and during this process there is a possibility to damage normal tissue cells. Ionizing radiation can be categorized based on how ionization occurs (11):

- Directly ionizing: electrons, protons and heavy particles; and

- Indirectly ionizing: photons and neutrons.

Directly ionizing radiation deposits energy through coulomb interactions between the charged particle and the medium. Indirectly ionizing radiation requires an extra step where the photons or neutrons interact with the medium and release a charged particle. This charged particle then deposits energy in the same way directly ionizing radiation does.

 While both types of ionizing radiation are used in radiotherapy for treatment, indirectly ionizing radiation remains the more commonly used method with over 11,440 linacs installed in over 139 countries compared to 115 heavy particle accelerators over 17 countries (12,13).

Indirectly ionizing radiation with photons can be further separated into four categories based on their origin (11):

- Characteristic X-rays emitted through electron transitions of between electron shells.

- γ-rays emitted as a result of a nuclear decay.

- Annihilation radiation resulting from a positron-electron annihilation.

- Bremsstrahlung photons produced by an electron-nucleus interaction.

A photon has a probability of interaction with the medium through which it is passing. The possible interactions with the medium depend on the atomic number of the medium and energy of the photon. **Figure 1.1** shows the regions where a particular photon interaction is dominant depending on the atomic number of the medium and the energy of the photon. In the energy range of radiotherapy (4-25 MeV) and in tissue ($Z_{eff} = 7.5$), the most common photon interaction is predominantly the Compton effect.
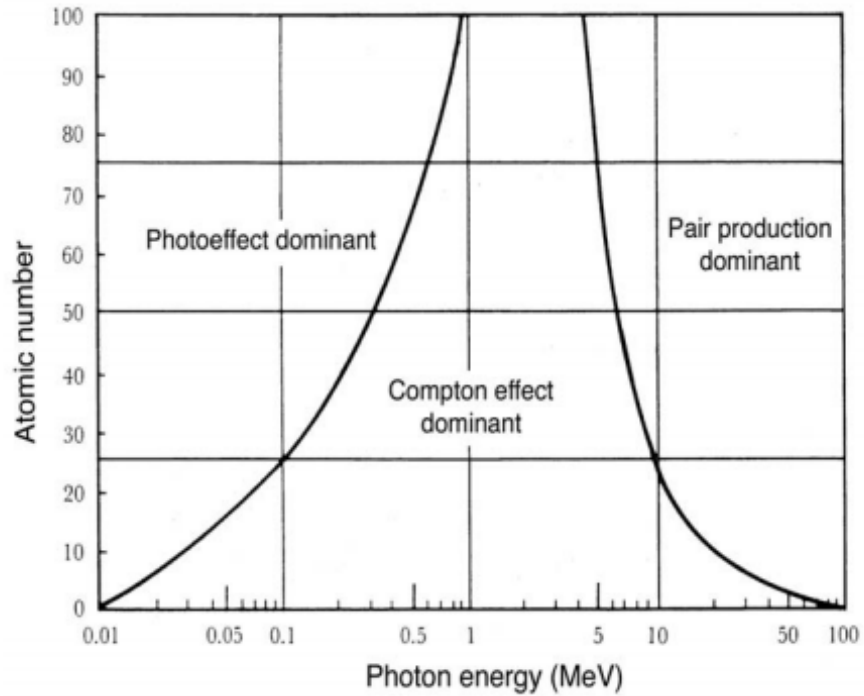
Figure 1.1 Photon effect dominance depending on photon energy and atomic number. The curves represent the region where there is equal probability of either effects occurring (11).

1.2.3 Medical Linacs

Medical linacs use high-frequency electromagnetic waves to accelerate electrons to high energies. These high energy electrons are then directed toward a target where they produce the photons used for treatment. **Figure 1.2** shows the block diagram of a linear accelerator.
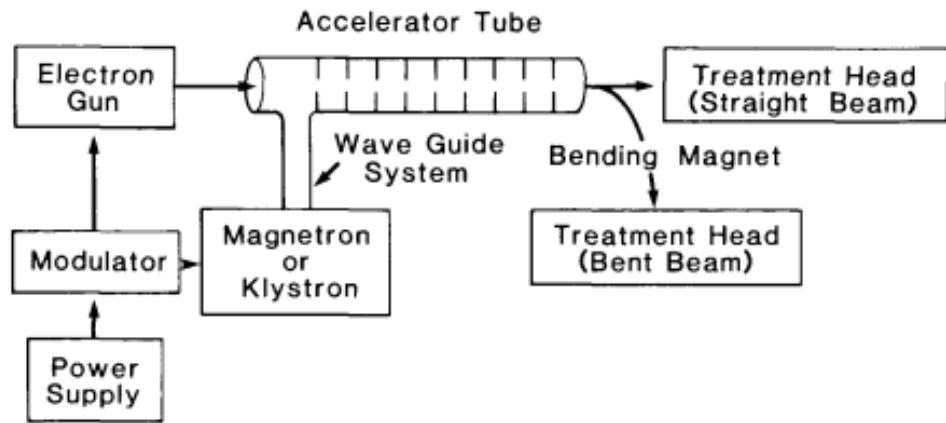
Figure 1.2 Block diagram of a typical medical linear accelerator (14).

First the electron gun injects the electrons to be accelerated in the accelerating waveguide. The Klystron, an RF amplifier coupled with an RF generator, or a Magnetron, an RF power source, produce high frequency microwaves (~3000 MHz). This RF power source, in conjunction with a modulator, accelerate the electrons inside the accelerating waveguide. The length of the accelerating waveguide determines the maximum energy which the electrons can reach. The electron beam then leaves the accelerating waveguide and in some cases, the beam is steered with a set of bending magnets, towards the target where the striking electrons will produce the resulting photons to be used during treatment.

Inside the treatment head of the linac there are several components that help shape the cross-section of the intensity of the photon beam to produce the desired treatment beam, measure the beam output and shield from any scattered radiation that may be produced when the photon beam interacts with any components in its path.

After production in the target, the first component with which the photon beam interacts is the flattening filter. This filter is used to attenuate the exiting photon beam

7

through preferential attenuation in the centre of the field to produce a flat beam at a predetermined depth in water (usually 10 cm). **Figure 1.3** shows the beam profile of a photon beam at 10 cm depth and 100 cm SSD, produced by a 25 MeV electron beam hitting a lead and aluminum target with and without a flattening filter.
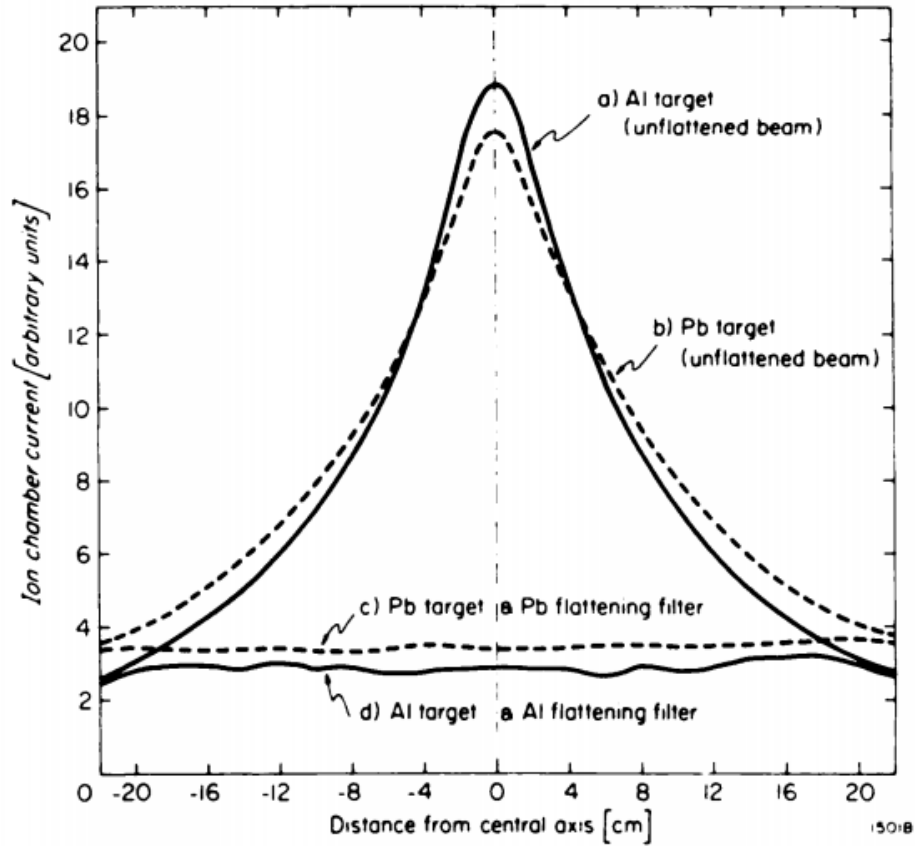
Figure 1.3 Comparison between unflattened and flattened photon beams produced by 25 MeV electrons (15).

The use of a flattening filter can be omitted for special treatments such as SRS (discussed in section 1.3), where the filter is frequently removed to produce a photon beam with a higher dose rate (16,17). Removal of the flattening filter from the path of the

treatment beam also results in a softer beam where photons of lower energies that would be attenuated are now able to deposit dose to the patient.

The primary collimator is used to define the largest available circular field size. The conical opening is machined from tungsten and the edges of the collimator project onto the edges of the target and the edges of the flattening filter. The thickness of the collimator is designed to attenuate the primary photon beam intensity to less than 0.1 % of the initial value (18).

The secondary collimation is used to define the maximum field size at the isocentre. The isocentre is the point in space relative to the treatment machine about which various components of the linac rotate. It consists of four independent jaws made of tungsten that define square and rectangular fields, typically with a maximum dimension of 40 x 40 cm^2. The jaws are able to rotate about their axis and the edges of the jaws are parallel to the beam at all angles.

Tertiary collimation can be included in the head of a linear accelerator using a multi-leaf collimator (MLC). The MLC consists of, for example, a bank of 60 pairs of tungsten leaves with 120 individually computer-controlled motors that cover the maximum field size defined by the secondary collimator. These leaves provide an efficient system to create irregular fields during treatment (18). There are different versions of MLCs that use smaller leaves for the innermost pairs that allow for highly conformal therapies such as SRS and SBRT. These banks of MLC leaves measure 2.5 mm in width for the innermost pairs and 5 mm for the peripheral bank of leaves.

The gantry and treatment couch axes intersect at a fixed point called the mechanical isocentre. The gantry rotation defines a horizontal axis which cuts a vertical axis defined by the rotation of the treatment couch. The treatment collimators also rotate about an axis passing through the isocentre. Given the mechanical tolerances of the equipment, this point in space is more accurately represented by an ellipsoid of one to two millimetres in diameter in largest dimension. The standard distance from the radiation source in the head of the linac gantry to isocentre is 100 cm and is referred to as the source-to-axis distance (SAD). The radiation isocentre is the point where the radiation beams intersect if the gantry, collimator or couch are rotated. The linac must be aligned so that both mechanical and radiation isocentres coincide. The patient to be treated is positioned at isocentre, if there are any discrepancies in the coincidence of the isocentres, the delivered dose can be outside of the planned treatment volume and could be harmful for the patients. This becomes critical in hypofractionated radiation treatments where patient position plays a major role during treatment (19). Hypofractionated radiation therapy employs a treatment schedule in which the total dose of radiation is divided into large doses and treatments are given less often than conventional radiotherapy.

1.2.4 Photon Therapy Modalities

There is a wide variety of treatments that make use of the technologies available in external-beam photon radiation therapy.

Stationary beam treatment consists of placing the isocentre of the linac at a depth within the patient and directing the beams from different directions. The SAD remains

constant for all beams at different angles. Stationary beam treatment can be done with one, but more commonly an arrangement of multiple intersecting beams. Increasing the number of beams for treatment generally delivers a lower dose to a higher volume of normal tissue. When collimation is used to customize the apertures of beams, a three-dimensional dose distribution can be tailored to conform to the target volume. This approach, called 3D conformal radiation therapy involves the use of static beams or beam arcs, where the MLC is shaped according to the projection of the target volume at each angle of incidence. 3D conformal radiation therapy spares healthy tissue around the tumor from the damaging effects of radiation, using 3D patient dataset information.

Intensity modulated radiation therapy (IMRT) is a treatment method that involves changing the beam intensity profile using MLCs to modulate the dose delivered to the patient from any given position of the treatment beam (14). The gantry is positioned at fixed angles based on the treatment plan and the MLCs are used to define the aperture of the beam. Each beam treats only a portion of the target volume at a time and allows for the sparing of healthy tissue. In 2004 a random survey reported that IMRT in the U.S. corresponded to 73.2 % of radiation therapy treatments (20).

Volumetric modulated arc therapy (VMAT) is a modality where treatment occurs during gantry motion, i.e. the MLC apertures are continuously changing throughout a full gantry rotation. VMAT optimizes the MLC leaf positions as well as weights for each beam aperture during the gantry rotation (21). VMAT also regulates the gantry speed and dose rate based on the objectives established by the user in the optimization process. VMAT also offers additional advantages, such as reduced treatment delivery time compared with

conventional IMRT. VMAT treatment delivery times are between 35-60 % shorter compared to IMRT (22).

Stereotactic radiosurgery (SRS) is a highly precise, single fraction technique that delivers high, ablative doses using stereotactic principles for target localization for treatment of intracranial lesions. Given that SRS is the focus of the technology described in this thesis, it is described in further detail in the next section.

1.3 STEREOTACTIC RADIOSURGERY (SRS) AND STEREOTACTIC RADIATION THERAPY (SRT)

SRS is a radiation therapy treatment that employs the same general principles of standard radiotherapy but involves delivery of a single fraction of dose to ablate tumors. The tolerances required for SRS are more demanding than for conventional RT and in particular, the technique requires steep dose gradients to reduce injury to adjacent normal tissue. Furthermore, SRS requires more stringent margins in both dose delivery and positional accuracy given that stereotactic radiation is commonly applied to lesions proximal to radiosensitive structures. The positional accuracy margins should be within ± 1 mm and can be affected by three factors: accuracy of target determination, accuracy of dose delivery and motion of the target structures after target localization and during treatment (18). A related technique is Stereotactic Radiation Therapy (SRT), which involves the same tolerances but fractionates the dose to spare proximal normal tissues.

SRS was first introduced in early 1950's by Lars Leksell, a Swedish neurosurgeon, along with his physicist colleague, Borje Larsson. Leksell and Larsson used 200 kVp x-rays to deliver high radiation doses in a single session to an intracranial target (18). Given

the limitations of the orthovoltage x-rays, Leksell used a cobalt-60 machine designed specifically for SRS treatments called the Gamma Knife (14). In the 1980's SRS was translated to linac platforms with the earliest report of linac SRS treatment published in 1989 (18).

Linac-based SRS treatment involves using multiple non-coplanar beams or arcs converging on to the machine isocentre. It is most commonly used in the treatment of brain or spinal tumors and brain. SRS requires the use of a head frame or other rigid device to immobilize the patient during treatment to ensure that the high dose of radiation is delivered accurately.
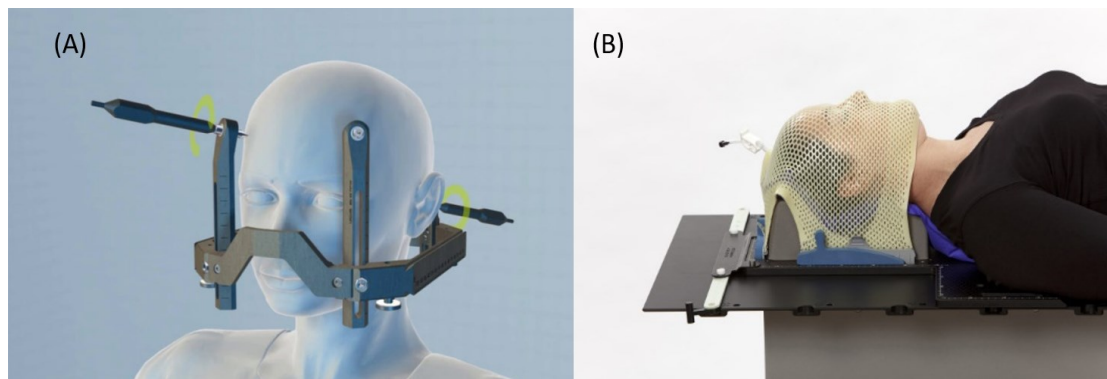
Figure 1.4 (A) Rigid head-frame immobilization (23) **and (B) Thermoplastic mask used for immobilization** (24)**.**

There are two main types patient immobilization for SRS (see Figure 1.4). The first is a stereotactic head frame, which includes a rigid ring fastened to the patient's head with pins placed in the outer table of the skull. Frame-based radiosurgery also involves attachment of a localizer box for imaging to define a coordinate system around the cranium,

for treatment planning purposes. **Figure 1.5** shows the localizer box used in frame-based radiosurgery. This coordinate system provides a unique relationship between the frame and the brain. At the time of treatment delivery, the localizer box is replaced with a target positioner box enabling the alignment of the patient's anatomy, defined by the stereotactic coordinate system, to the coordinate system of the treatment unit. The origin of the frame may be aligned with the isocentre of the linac to within 0.2 mm (14).
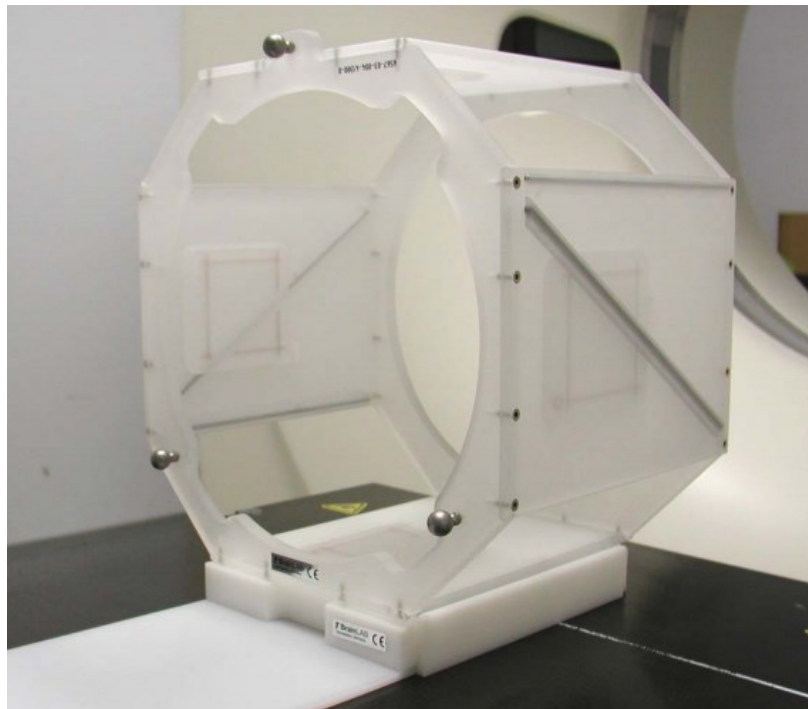
Figure 1.5 Localizer box used to a define coordinate system around the cranium.

Frameless radiosurgery is less invasive with regard to the patient immobilization used, but the goal is to avoid compromising the spatial accuracy compared to frame-based methods (18). The frameless approach requires a rigid and relocatable mask system that conforms to patients head to limit movement. While the frameless design provides a less

invasive immobilization system, it has been shown to allow patient motion between 0.5-2 mm during treatment (25–29).

1.3.1 Patient Motion during SRS

Motion during frameless SRS, if significant in magnitude, can lead to geographic miss of the target volume and irradiation of healthy tissues given the small margins used in treatment planning. Peng et al. showed the average variability in patient position during treatment was within ±0.4 mm/0.4º and approximately ±1 mm/1º. **Figure 1.6** shows an example of the intrafractional motion a patient experiences during the initial CBCT acquisition and during treatment at different couch and gantry angles. During patient treatment Peng et al. showed that there can be motions of up to 3 mm. It is this type of motion that can have a large impact in accurate treatment delivery.
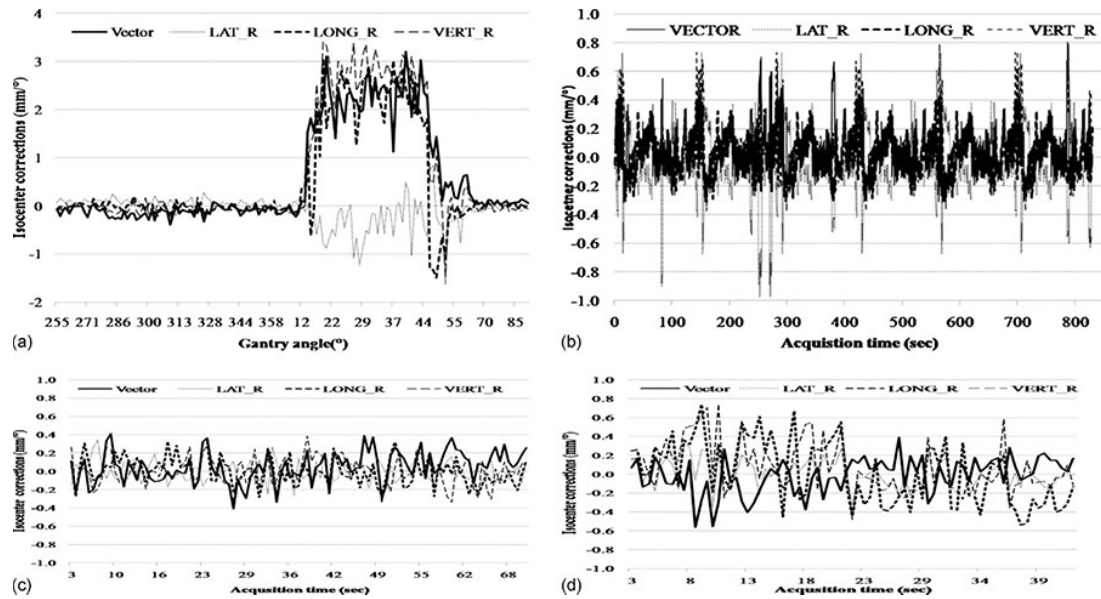
Figure 1.6 An example of the intrafractional motion of the AlignRT (a) during CBCT acquisition and treatment delivery at (b) couch 0° and gantry angles of 120°, 90°, 45°, 315°, 270°, and 240°; (c) couch 55° and gantry 120°; and (d) couch 270° and gantry 300°, respectively. (30)

Gevaert et al. performed a study to evaluate a robotic 6-degree of freedom treatment couch for frameless radiosurgery. It was found that for 9 of the 66 lesions, the intrafractional motion was larger than 1 mm, which was the tolerance limit for approving the treatment. While the mean 3D deviation for the patient population was 0.58 mm (SD, 0.42 mm) it is the outliers that become a concern for high dose treatments. Similarly, 18 of 66 lesions experienced a rotation larger than the treatment tolerance (0.5°). **Figure 1.7** shows the intrafraction shifts and rotations errors at the end of treatment.
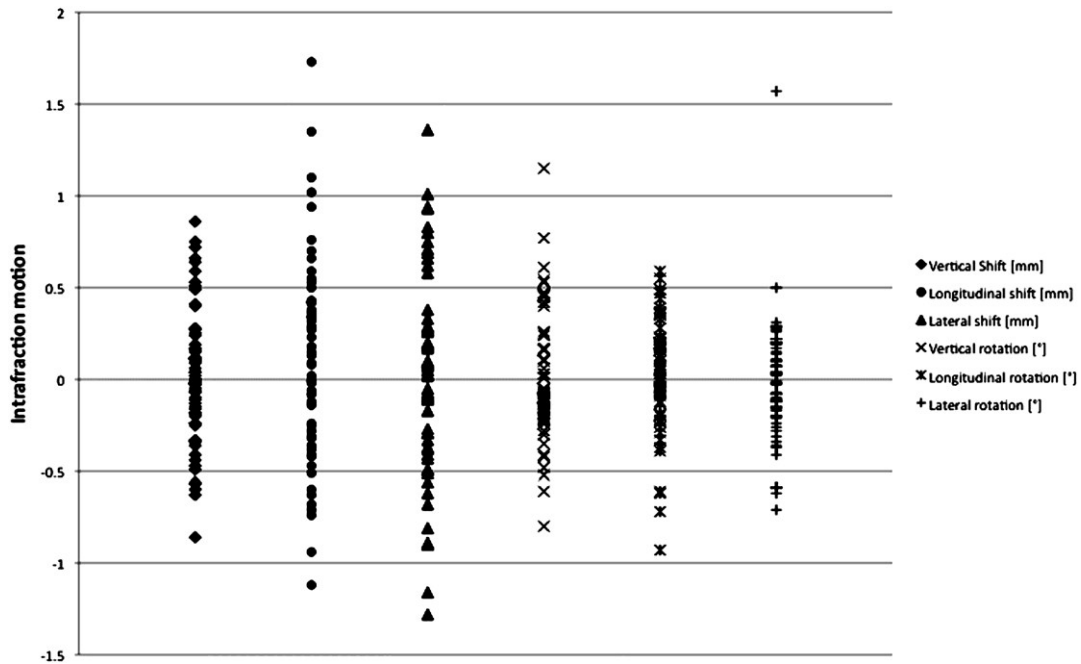
Figure 1.7 Residual errors or intrafraction patient motion measured directly after treatment was finished (31)**.**

Opp et al. monitored patient motion of 77 subjects before treatment using frameless immobilization. The results of the study showed that patient position degrades as time passes with 90 % of patients remaining within 1 mm of the reference position for up to 291 seconds, 80 % for up 443 seconds and 70 % for up to 667 seconds during the 15 minutes of observation (32) .

Ramakrishna et al. performed a study to compare intrafraction motion between frame based SRS against a frameless system. It was found that the mean intra-fraction shift for patients immobilized with the frameless system was 0.7 mm (SD = 0.5 mm). Meanwhile, the frame based treatments the mean intra-fraction shift was 0.4 mm (SD = 0.3 mm). This study also found that 22 % of those immobilized with a mask displayed shifts of 1 mm or greater compared to 3 % with a fixed frame. **Figure 1.8**A shows the

shifts during treatment and **Figure 1.8**B shows a histogram representing the 3D

displacement magnitude for both types of immobilization.
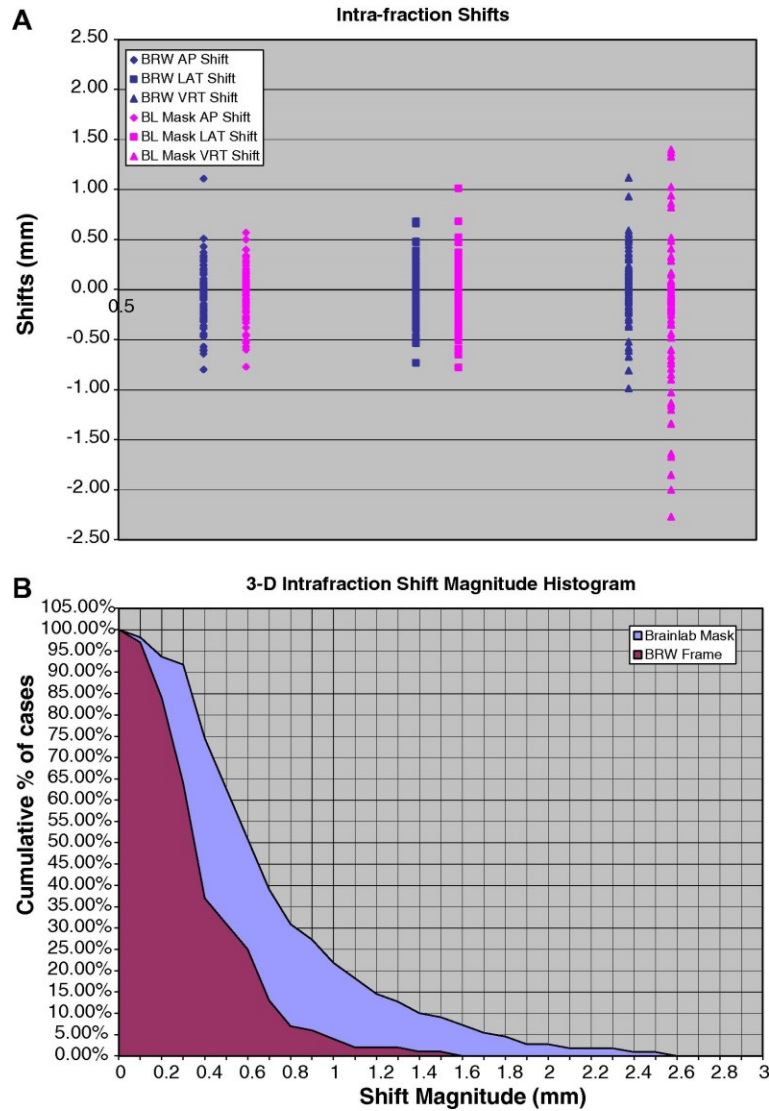
Figure 1.8 Intra-fraction shift: frame-based versus mask-based immobilization: (A) The mean AP, VRT and LAT components of intra-fraction displacement determined by the image-guidance system of patients immobilized using either the fixed head frame (BRW) or the frameless system (BL). (B) A histogram of the 3D intra-fraction displacement

magnitude for patients immobilized using either the frameless system or the fixed head frame (33)**.**

SRS is often used for the treatment of multiple central nervous system metastases using a multi-isocentre set up, sequentially aligning each isocentre to individual metastatic lesions. This approach can result in a protracted treatment delivery time which scales according to the number of lesions. As discussed previously, as treatment time increases, patient positioning degrades resulting in high doses delivered to healthy tissues. This has prompted the use of single-isocentre treatment of multiple metastases to reduce treatment time and increase patient convenience (34,35). However, this type of treatment increases the potential severity of intra-fraction patient motion given that a small rotational error can lead to significant dosimetric degradation especially for lesions located distant from the treatment isocentre (36). Gevaert et al. suggest that thresholds of 1 mm and 0.5° are sufficient to assure accurate treatment delivery (31). This motion during treatment can greatly affect the delivered dose and therefore real-time monitoring of the patient is required when the frameless immobilization is used (37–39).

According to a retrospective study on the effect of intrafraction motion in spine SRS, motions greater than 2 mm can cause significant deviations from planned tumor dose, with the error proportional to the motion magnitude. In this study, for motions deviating more than 2 mm from the original planned position, doses were recalculated using the treatment planning system and it was found that for one plan out of 20, the dose delivered violated criteria for PTV coverage (37).

1.3.2 Patient Position Monitoring for SRS

Given the advantages to the patient of the frameless approach, and the strict requirements for spatial accuracy, there exist multiple monitoring systems available that can be used for SRS. These include Cone Beam Computed Tomography (CBCT), stereoscopic imaging, surface imaging and implantation of markers or beacons. **Figure 1.9**A shows the CBCT system in a linac, **Figure 1.9**B shows the stereoscopic system inside a treatment room, and **Figure 1.9**C shows a treatment room with surface imaging cameras.
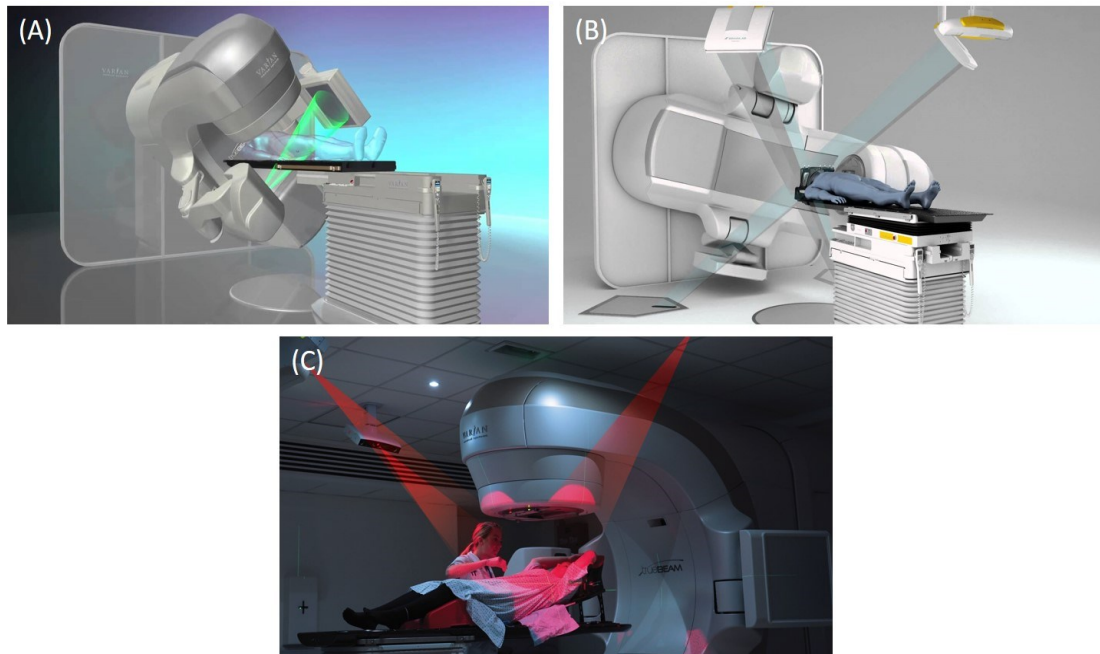
Figure 1.9 (A) CBCT system used in Truebeam linacs (Varian Medical Systems, Inc., Palo Alto, CA) (40)**, (B) ExacTrac Stereoscopic imaging system (Brainlab AG, Munich)**(41)**, (C) AlignRT surface imaging monitoring system (Vision RT Ltd, London, England)**(42)**.**

CBCT involves the use of a gantry-mounted flat panel imager to acquire a sequence of projection images as the gantry is rotated around the patient. The radiation source can be either a kV x-ray tube (kV CBCT) or the MV beam from the linac (MV CBCT). A full 3D image dataset of the patient is reconstructed, similar to that produced by conventional CT. CBCT is used as a patient positioning system that is now included in most modern linac platforms (43). The 3D image set of the patient allows for visualization of the patient anatomy compared to the reference conditions, i.e., the treatment planning CT; shifts and rotations can then be determined for patient alignment.

While CBCT provides a readily available positioning system for SRS, it has some disadvantages. CBCT is not real-time, with acquisition and reconstruction requiring approximately one minute, and the accuracy is subject to the mechanical tolerances of the arms supporting the source and detector on a rotating gantry (44). According to Chang et al., CBCT accuracy for patient positioning is on the order of 1 mm for fixed frame SRS treatments (45), i.e., the accuracy of the positioning system is close to the desired tolerance for treatment delivery itself. Chang et al. also concluded that if frameless SRS is to be used, then CBCT must be used alongside a motion detection system to determine and apply any correctional shifts to the treatment table.

Stereoscopic imaging involves the use of two orthogonal, planar x-ray imaging systems integrated in the treatment room; visualization of the same anatomy in both planar images allows calculation of the 3-dimensional coordinates of landmarks. Projection images are co-registered with reference digitally reconstructed radiographs (DRRs) generated from the treatment planning CT image data. Image acquisition does

21

not necessarily require treatment interruption, and thus it can image the patient to detect

intrafraction motion provided that the imaging view is not blocked by the linac gantry. In

addition to the thermoplastic mask, a localizer frame with infrared markers is attached to

the treatment couch and monitored using cameras during treatment. This system can be

used to align the patient to the correct treatment position prior to initiating treatment

delivery, followed by periodic imaging. Commercial implementations, e.g., ExacTrac

(Brainlab AG, Munich) and the imaging system for Cyberknife (Sunnyvale, CA, USA)

allow intra-fractional imaging but acquisition is not continuous. Stereoscopic x-ray

systems such as the Brainlab ExacTrac image-guidance system have a reported accuracy

between 0.5 and 1.5 mm (46–48).

Stereoscopic image guidance systems involve several disadvantages. First, the

anatomy visualized in stereoscopic projections consists primarily of bony landmarks or, if

implanted, fiducial markers, with soft tissue being difficult to visualize and co-register

with reference images (49). Since ionizing radiation is required, this adds inadvertent

dose to a fairly high volume of anatomy of the patient, and this dose increases if near-

real-time monitoring is required (50,51).

Surface imaging and registration techniques use a ceiling mounted 3-D optical

camera for real time tracking (52). These systems monitor a region of interest on the

surface of the patient during patient setup or treatment delivery and do not require

administration of ionizing radiation. Surface imaging uses skin as a surrogate for the

tumor in an effort to determine whether the target volume has shifted during the course of

treatment. For monitoring of the cranium, this typically requires the thermoplastic mask

to have a cutout over the region of the skin that will be monitored. **Figure 1.10** shows an example of an open-face mask compatible with surface imaging.

Figure 1.10 Open-face mask ClearVision 2 Type-S (CIVCO Radiotherapy, Orange city, IA) used for patient immobilization compatible with surface imaging tracking (53)**.**

Align RT (Vision RT Ltd, London, England) is an optical surface imaging system that can be used for patient positioning and for motion detection during treatment. The ceiling mounted cameras capture an initial static image that is used for positioning. For motion tracking the system captures images sequentially. While surface imaging provides a non-invasive, real-time motion detection system, the use of skin as a surrogate for tumor motion can lead to false positive motion detection events (54).

Surface imaging for SRS guidance involves imaging a limited area of the head surface causing a bias in the anterior surface alignment due to the lack of cameras in the anterior part of the head (54). The system's accuracy can be affected by facial

expressions and weight changes between simulation and treatment (30,54). Several studies suggest that a surface imaging system such as AlignRT can achieve an accuracy of less than 1 mm when used with a modified frameless design for SRS (29,54,55) This modified frameless design uses a head mold and a personalized mouthpiece that reduces facial motion when compared to the open-face mask commonly used in surface imaging (54). Furthermore, this modified frameless design causes mild skin stretching and is less likely to deform during treatment (29).

As an alternative approach, passive radiofrequency markers or beacons can be implanted in the cranial region and monitored in near real-time using the Calypso 4D localization and Tracking System (Varian Medical Systems). The Calypso system uses electromagnetic transponders implanted in the tumor or the skin for improving setup accuracy and for accounting for intrafraction motion inside the frameless patient immobilization system (56). The reported accuracy for the implantation of markers or beacons for tracking system is less than 1 mm (56–58). The application of this approach to cranial monitoring is quite rare given the associated invasiveness and cost.

In summary, while a range of patient monitoring systems for SRS exists, each approach involves particular strengths and weaknesses, as summarized in **Table 1.1**

Table 1.1 Summary of available patient position monitoring systems for SRS.

Patient position monitoring system	Imaging Acquisition	Temporal resolution	Additional dose	Accuracy	Caveats
CBCT	3D	Poor, greater than 1 minute	5-36 mGy per image (59)	≤1 mm	Can only be used for patient positioning before and after treatment.
Stereoscopic X-ray	2D, with calculation of 3D coordinates	20 Hz (47) however commercial systems do not support this	0.5 mGy per image (60)	<1 mm	Additional dose to the patient, limited temporal resolution, requires modification of treatment room to setup x-ray detectors.
Optical surface imaging	3D	6.5 Hz (55)	No additional dose	<1 mm	High capital investment, skin is used as a surrogate leading to false positive detection, need to compromise mask for SRS monitoring.
Implanted markers or beacons	4D	10 Hz (61)	No additional dose	<1 mm	Invasive procedure

1.4 RESEARCH GOALS

The main goal of this research is to demonstrate that the principle of capacitance can be used to detect cranial motion during SRS treatment by developing a detector providing acceptable spatial resolution, stability and signal-to-noise characteristics. The proposed system relies on the change in capacitance that occurs when the distance between the cranium and the detector changes. This technology, which is now patent pending (62), must satisfy criteria that will make it compatible to intra-fraction monitoring during SRS, specifically:

(1) Sub-millimetre spatial resolution.

(2) Capacity to read out the position of the patient in real-time, or near real-time.

(3) Absence of unwanted ionizing radiation.

(4) Ability to monitor the position of the cranium as a whole.

(5) Sensitivity to the cranial position, while being comparatively insensitive to the position of the mask surrounding the cranium.

(6) Absence of highly attenuating materials in the paths of the incoming radiation beams.

In this work, the design of a novel capacitive detector is presented. The detector incorporates a capacitive plate that will be located proximal to the cranium. The relevant variables in the design of this detector, such as detector size, material and shape, are explored and optimized. This is a key phase of research and development toward a

system that will include multiple detector elements and will provided three-dimensional

patient monitoring.

CHAPTER 2 CAPACITANCE PHYSICS

2.1 INTRODUCTION

Capacitance is the property of a conductor or a system of conductors to store charge. The fundamental relationship between charge (Q), capacitance (C), and voltage potential (V), is given by equation (1). The energy stored in a capacitor is given by equation (2). From these equations it is apparent that the charge and therefore energy storage capability increases with capacitance.

$$Q = C \cdot V \tag{1}$$

$$W = \frac{1}{2}CV^2 \tag{2}$$

Capacitance exists whenever two conductors are in sufficient proximity. A capacitor is a passive two-terminal electrical component that stores electrical energy in an electric field. The simplest capacitor arrangements have two conductive plates separated by only a thin layer of insulator (dielectric). When one plate is charged negatively and the other charged positively, more electrons can be stored since the electrons on the negative plate are drawn to the holes on the positively charged plate. A smaller gap between the plates produces a higher capacitance. If the gap distance is variable, the capacitance between the two plates will vary as well.

When both conductors are in close proximity, one plate will be charged positively and the other negatively. In between both plates there will be a uniform electric field. This electric field is defined by equation(3).

28

$$E = \frac{V}{d} \tag{3}$$

Furthermore, the change in voltage is defined as the work done per unit charge. It can be calculated from the work done against the electric field. Equation (4) shows the relationship between voltage and work. Equation (2) can be derived from equation (4) by substituting V with equation (1) and integrating the resulting expression with respect to charge.

$$W = \int_0^Q V(Q)dQ \tag{4}$$

When a dielectric is introduced in the gap between the conductors, there is an increase in capacitance. Dielectrics are divided in two types: Polar and non-polar (63). A polar dielectric is made up of molecules that have a permanent electric dipole. Without an electric field the molecules are randomly oriented. When an electric field is present the molecules realign to create an electric field opposite to the original electric field but smaller in magnitude. This decrease in electric field results in an increase in capacitance.

Non-polar dielectrics have no permanent electric dipole. When in an applied electric field, the molecules of the dielectric experience an induced electric dipole moment. This induced electric dipole creates an electric field opposite to the applied field which reduces the initial strength of the electric field and consequently increases the capacitance of the capacitor.

Figure 2.1 shows how the electric field rearranges the electric dipole of the

dielectric material. The induced electric field from the dielectric reduces the magnitude of

the initial electric field, which decreases voltage between conductors, resulting in an

increase in capacitance.
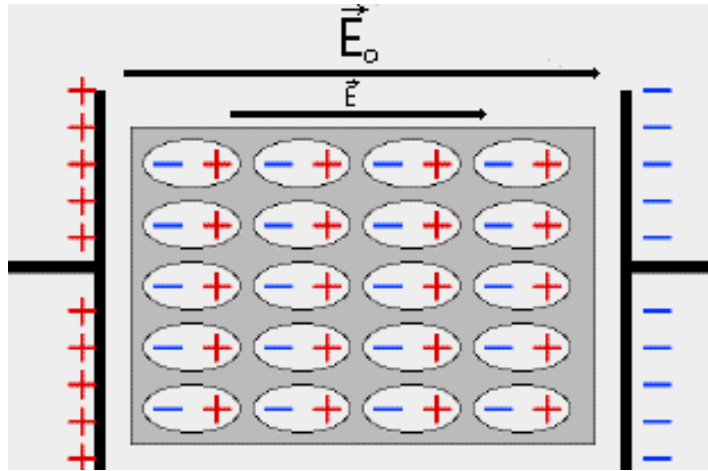
Figure 2.1 Diagram showing reduction of the electric field E_o when a dielectric is placed in between two conductors.

The effectiveness of either type of dielectric depends on the polarizability of the

material. A polar material with rigidly-held molecules in a lattice may not have a very

high dielectric constant. An example of a polar material with a high dielectric constant is

water. The molecules in water will easily align with an external field and result in high

polarization. On the contrary diethyl ether is a polar material that has a low dielectric

constant.

A key property of a dielectric is the breakdown voltage. The breakdown voltage is

the minimum voltage that causes a portion of an insulator to become electrically

conductive. The breakdown voltage of a material is not a definite value. It a value at

which there is a statistical probability that the material will fail at a given voltage. The breakdown voltage of air is 3 kV/mm. At this voltage air will begin conducting electricity rather than acting as an insulator. The voltages used for this system are several orders of magnitude smaller than the breakdown voltages of air.

Capacitance sensors have been used commercially for high sensitivity non-contact measurements (64) given the use of either a varying gap or varying area to change their capacitance as a function of displacement.

2.2 PARALLEL PLATE CAPACITORS

The capacitance of an idealized parallel plate capacitor has a simple closed-form solution, shown in equation (5). The capacitance is directly proportional to the surface area (A) of each plate, the permittivity of free space (ε_o), the relative permittivity of the dielectric between the plates (ε_r), and inversely proportional to the distance between plates (d). The permittivity of free space has a value of 8.854×10^{-12} F/m. The relative permittivity is a dimensionless quantity greater than 1 that relates the permittivity of the medium between the plates to that of vacuum. If air is the dielectric material between the plates $\varepsilon_r \approx 1$ at standard temperature and pressure conditions (65).

$$C = \frac{\varepsilon_0 \varepsilon_r A}{d} \tag{5}$$

This relationship is considered only a first order approximation since it neglects fringe effects. It assumes that the electric field is perfectly uniform across the gap between the plates and is zero elsewhere.

31

Under the assumption of a uniform electric field and that charges in the conductors remain stationary, the electric field expression from Maxwell's equations is simplified to equation (6) where the electric field is equal to the resistivity of the material divided by the permittivity of free space.

$$E = \frac{\rho}{\varepsilon_0}$$ (6)

The relationship between voltage and electric field in a capacitor can be derived using equations (3) and (6) where the change in voltage is defined as the work done per unit charge against the electric field.

$$\Delta V = \int_0^d E \cdot ds$$ (7)

$$\Delta V = \frac{\rho}{\varepsilon_0} d$$ (8)

Furthermore, equation (1) can be rewritten using equation (9) and rewriting Q in terms of conductivity and area. This rearrangement is used to derive equation (5). Note that $\rho = \frac{1}{\sigma}$ where σ is the conductivity of the material.

$$C = \frac{\varepsilon_0}{\sigma d} \sigma A = \frac{\varepsilon_0 A}{d}$$ (9)

Capacitive monitoring with parallel plates offers many advantages. The capacitive sensing system responds to average displacement of a large area of a moving electrode,

32

thereby providing a robust measurement in practice (66). This sensing method also has a high signal to noise ratio. An important feature of capacitive monitoring is that it is less sensitive to lateral movement or misalignment of the plates, especially when the area A is large and thus it can respond to motion along the axis perpendicular to the plates and minimize the effect of slight motion parallel to the plates(66).

A dielectric can be used in between a parallel plate capacitor. As shown in equation (5), introducing a dielectric with a high dielectric constant will result in an increase in capacitance. There are several materials that can be used as a dielectric. **Table 2.1** lists materials and corresponding dielectric constants. Using **Table 2.1** it is possible to select a dielectric with a high dielectric constant. This in practice is more complicated. Depending on the application using some of these materials can be dangerous or impractical. The dielectric constant of the human body depends on the frequency at which it is being measured. At 100 kHz the dielectric constants of muscle, fat and bone are 113, 20 and 7.3 respectively (67). The materials used to create thermoplastic masks have a dielectric constant between 1.5 and 3.5.

Table 2.1 Dielectric constants (66).

Material	Dielectric Constant		Material	Dielectric Constant
Acetone	19.5		Paper	1.6-2.6
Acrylic resin	2.7-4.5		Perspex	3.2-3.5
Air	1.000264		Petroleum	2.0-2.2
Alcohol	25.8		Phenol Resin	4-12
Ammonia	15-25		Polyacetal	3.6-3.7
Aniline	6.9		Polyamide	5.0
Aqueous solution	50-80		Polyester resin	2.8-8.1
Bakelite	3.6		Polyethylene	2.3
Benzene	2.3		Polypropylene	2.0-2.3
Carbon sealing compound	2.5		Polystyrene	3.0
Carbon dioxide	1.000985		Polyvinyl chloride resin	2.8-3.1
Carbon tetrachloride	2.2		Porcelain	3.5-4
Celluloid	3.0		Powdered milk	3.5-4
Cement powder	4.0		Pressboard	3.7
Cereal	3-5		Quartz glass	3.7
Chlorine liquid	2.0		Rubber	2.5-3.5
Ebonite	2.7-2.9		Salt	6.0
Epoxy resin	2.5-6		Sand	3-5
Ethanol	24		Shellac	2.5-4.7
Ethylene glycol	38.7		Shell lime	1.2
Fired ash	1.5-1.7		Silicon varnish	2.8-3.3
Flour	1.5-1.7		Soybean oil	2.9-3.5
Freon R22, 502	6.11		Styrene resin	2.3-3.4
Gasoline	2.2		Sugar	3.0
Glass	3.7-10		Sulphur	3.4
Glycerine	47		Teflon	2.0
Hard paper	4.5		Toluene	2.3
Marble	8.0-8.5		Transformer oil	2.2
Melamine resin	4.7-10.2		Turpentine oil	2.2
Mica	5.7-6.7		Urea resin	5-8
Nitrobenzene	36		Vaseline	2.2-2.9
Nylon	4-5		Water	80
Oil saturated paper	4.0		Wood, dry	2-7
Paraffin	1.9-2.5		Wood, wet	10-30

2.3 MOTION DETECTION WITH CAPACITORS

Capacitive sensing is a term for a number of different sensing techniques that measure changes in capacitance. It can detect nearby objects by identifying the disruption to an electric field generated by a sensor. It can detect conductive objects or those having a significantly different permittivity than that of air, like a human body. The proximity sensing feature of capacitive sensors is used in numerous industries for detecting changes different properties such as acceleration (68), pressure (69), strain (70), position (71) and humidity (72) to name a few. Any change in capacitance is a result of a change in the distance between the probe and the target. When the object gets closer to the plate, the capacitance of the formed capacitor increases. One can measure the capacitance and from this calculate or estimate the distance between sensor plate and object. Objects partially consisting of conductive materials like metal or water are very well suited for tracking. In the case of the human body, there is no need to be grounded in order to act as a good capacitor plate mainly because the body itself provides a sufficient charge reservoir (73).

There are three different capacitive sensing methods: Loading mode, shunt mode and transmit mode. Loading mode is the basic mode capacitive sensing, where the capacitor plate and the object are unified in one electrode. A loading mode capacitive sensor measures the capacitance between its capacitor plate and the object, for example by completely charging this capacitor and discharging it. From the time needed to

completely discharge the capacitor, its capacitance can be calculated. This capacitive

sensing method is shown in **Figure 2.2**.
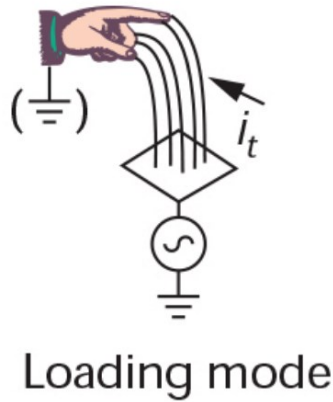
Loading mode

Figure 2.2 Diagram showing an example of loading mode capacitive sensing (73). **© [1998] IEEE.**

In shunt mode the resting electric field between two electrodes, the transmit and

receive electrodes, is "shunted" away from the receive electrodes by an object of interest,

e.g., a human finger, body, foot, metallic object, or any object that disturbs the field and

has a capacitive coupling to ground. **Figure 2.3** shows a diagram of the shunt mode

method of capacitive sensing.
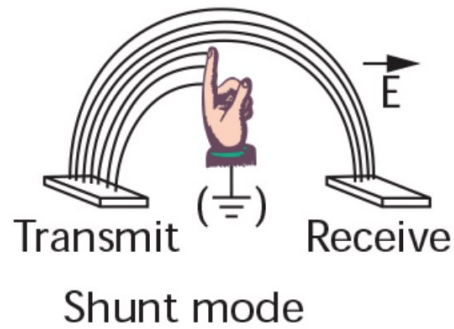
Figure 2.3 Diagram showing an example of shunt mode capacitive sensing where a finger is "shunting" the electric field (73)**. © [1998] IEEE**

In transmit mode the object-electrode capacitances are on the same order of magnitudes. Here, the object increases the electrode capacitance rather than shunting the field to ground and reducing that capacitance. **Figure 2.4** shows a diagram of the shunt mode method of capacitive sensing.
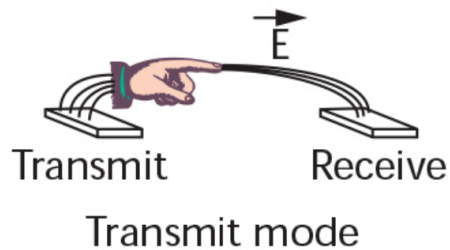
Figure 2.4 Diagram showing an example of transmit mode capacitive sensing. © [1998] IEEE

2.3.1 Human Body Capacitance

Capacitive sensing has been used for applications involving the human body. The capacitive sensor measures the capacitance distributed from the electrode to a human

37

body, where the human body has some capacitance with respect to grounding. When there is no object opposite to the electrode, the electric field lines are directed to the surrounding environment. When the human body approaches, an increase occurs in the density of electric field lines between the electrode and the human body. As a result, the capacitance sensing circuit measures the increased capacitance due to human proximity. An example of such systems is given by Togura et al. where objects such as dimming switches are dependent on the position of a human body relative to the sensor electrode that can be easily operated by simply moving a hand or a foot (74).

An application of a proximity sensor in industry was described by Nils Karlsson. His research used a capacitive sensor for the detection of humans in production lines that have robotic arms working at high speeds with many degrees of freedom (75). This was achieved using two conductive parallel plates in the ceiling and floor. A person entering the space between the plates of the capacitor will cause a change in capacitance.

Cheng et al. used the principle of capacitive sensing in a hospital setting to create an interface that can view and manipulate the patient's data on a bed side display without hindering the doctor's ability to interact with the patient (74). This was achieved with the use of a large area, textile, capacitor on body sensing for contact-less detection of control gestures.

CHAPTER 3 METHODS AND MATERIALS

In this chapter, the variables and the direct effect they have in the detectors are discussed. An overview of the acquisition system is discussed first, followed by the testing setup. Finally, a small volunteer study was performed to test the viability of the designs with the detector proximal to the cranium.

3.1 OVERVIEW OF EXPERIMENTS

For several detector designs, the variation in sensitivity (signal change per mm) was investigated with regard to:

1. The shape of the plate;

2. The area and thickness of the plate; and

3. The material of the plate.

The experiments were carried out using a parallel plate setup. In experiment 1, the effect of using three different shaped detector plates (square, circle and triangle) of similar area is investigated. Experiment 2 consists of three detector plate thicknesses (0.0762 mm, 0.127 mm and 0.254 mm) of copper and the effects of increasing detector plate size from 1x1 cm^2 to 10x10 cm^2 for all thicknesses. Finally, experiment 3 investigates the effect of using two different detector plate materials with different conductivities and how it affects the sensitivity of the system for three different detector plate dimensions.

3.2 ACQUISITION **S**YSTEM

The acquisition system consisted of a capacitive touch sensor breakout board (Adafruit MPR 121, Adafruit Industries, NYC, NY), an I2C interface device (NI USB-8452, National Instruments, Austin, TX), a detector made of copper or Mylar and an acquisition interface created in MATLAB. The process through which the data is acquired is shown in **Figure 3.1**.
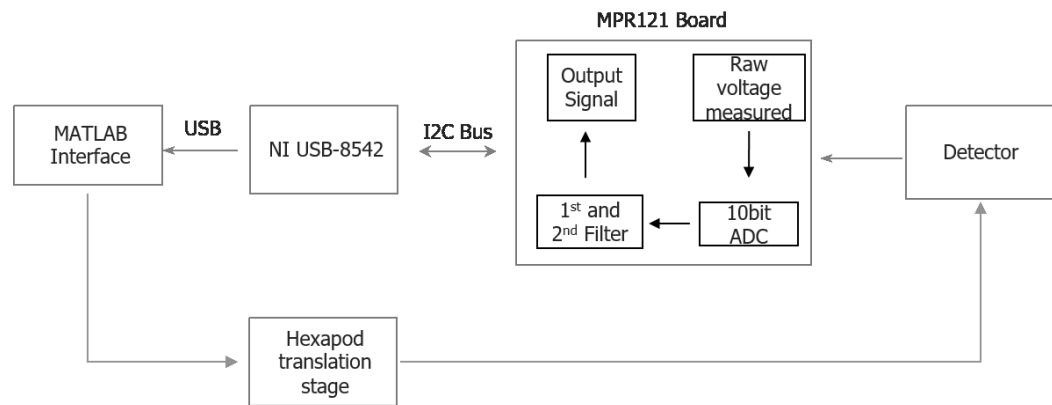
Figure 3.1 Block diagram of the acquisition process starting from the signal acquired by the detector and the data processing occurring inside the MPR121 Board. The MATLAB interface synchronizes translation motion and the start of the data acquisition with the NI USB-8452.

3.2.1 Adafruit MPR 121 Breakout Board

The Adafruit MPR 121 breakout board was chosen due to its low cost, availability of 12 input electrode channels and the I2C protocol that allowed for simple communication with the board through the appropriate serial bus. This board acquires an

analog signal through one of its sensing channels and converts it to a digital signal using

a 10-bit ADC. To measure the capacitance, the MPR121 uses a constant DC charge. The

selected electrode is charged and then discharged periodically to measure the capacitance.

This capacitance measurement includes the parasitic capacitance to ground and the

induced capacitance. Both charge current (I) and charge time (T) can be programmed to

optimize the capacitance values to be measured. The relationship between the analog

signal measured and the capacitance values can be calculated using equation (8) where

V_{dd} is the power supply input, in this case 3.6 V, I is the selected charge current and T the

selected charge time.

$$C = \frac{I * T}{ADC\ counts} * \frac{1}{V_{dd}} * \mathbf{1024} \tag{8}$$

As seen from equation, the selection of I and T directly affect the capacitance

values. However, determining the exact capacitance value was not a requirement for this

research; for the purposes of sensing changes in patient position, maximizing change of

capacitance was of primary interest. This prompted the use of equation (8) to quantify the

sensitivity of the system or the relative change in signal per unit distance.

$$S = \frac{\Delta signal}{\Delta distance} \left(\overline{signal}\right)^{-1} * \mathbf{100}\ \% \tag{9}$$

While the exact capacitance values were not essential, the values for I and T were

selected to allow the use of the full dynamic range of the device. This can be achieved by

maximizing the voltage supplied to the electrodes. However, the charge should not be so

high that the voltage exceeds the available values for the ADC. This prompted an investigation to determine the appropriate values to be used in the parallel plate experiments and volunteer study.

3.2.2 Charge Current and Discharge Time

The MPR121 board has an available range of charge currents between 1 and 63 µA, and charge durations between 0.5 and 32 µs. To determine the best combination of I and T, a set of tests with a parallel plate setup was performed. Using a 5x5 cm^2 copper detector plate and an opposing grounded 20x20 cm^2 copper plate, the charge current was varied from 1 µA to 63 µA while keeping the charge time fixed at 0.5 µs. The detector plate was displaced using a Hexapod translation stage (H-820, Physik Instrumente, Karlsruhe, DE) over a range of 8 mm. The experimental setup is shown in **Figure 3.2**. The detector plate is placed against a piece of acrylic attached to the Hexapod and displaced away from the grounded plate.
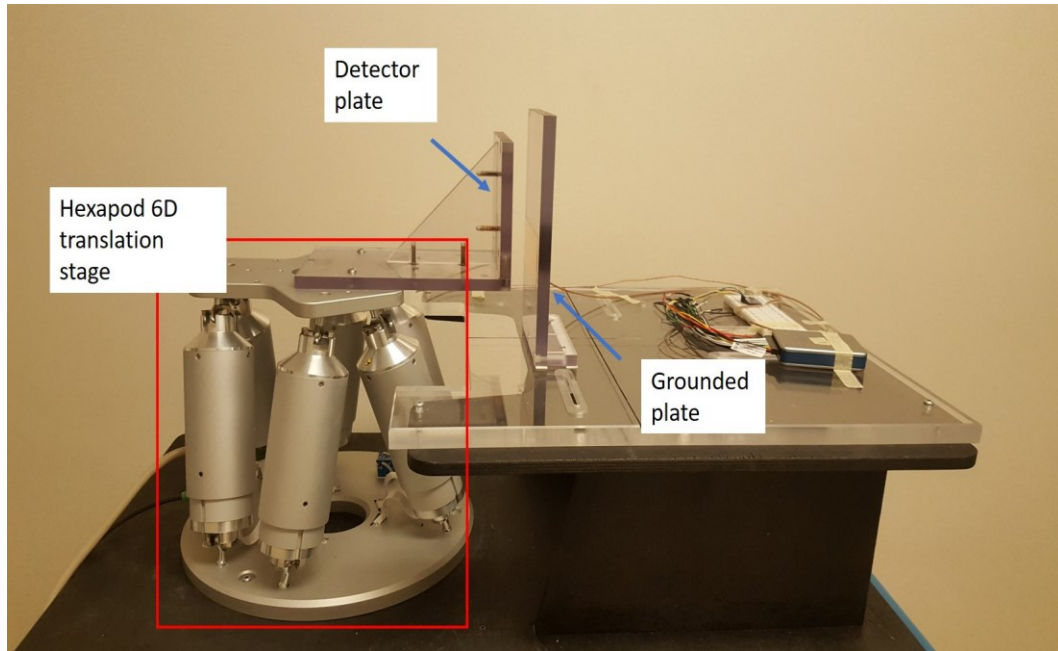
Figure 3.2 Experimental setup of parallel plate tests.

This setup allowed for the analysis of the effect of changing current to its maximum

value without saturating the ADC with a high charge time. The results of the test are shown

in **Figure 3.3**.

43
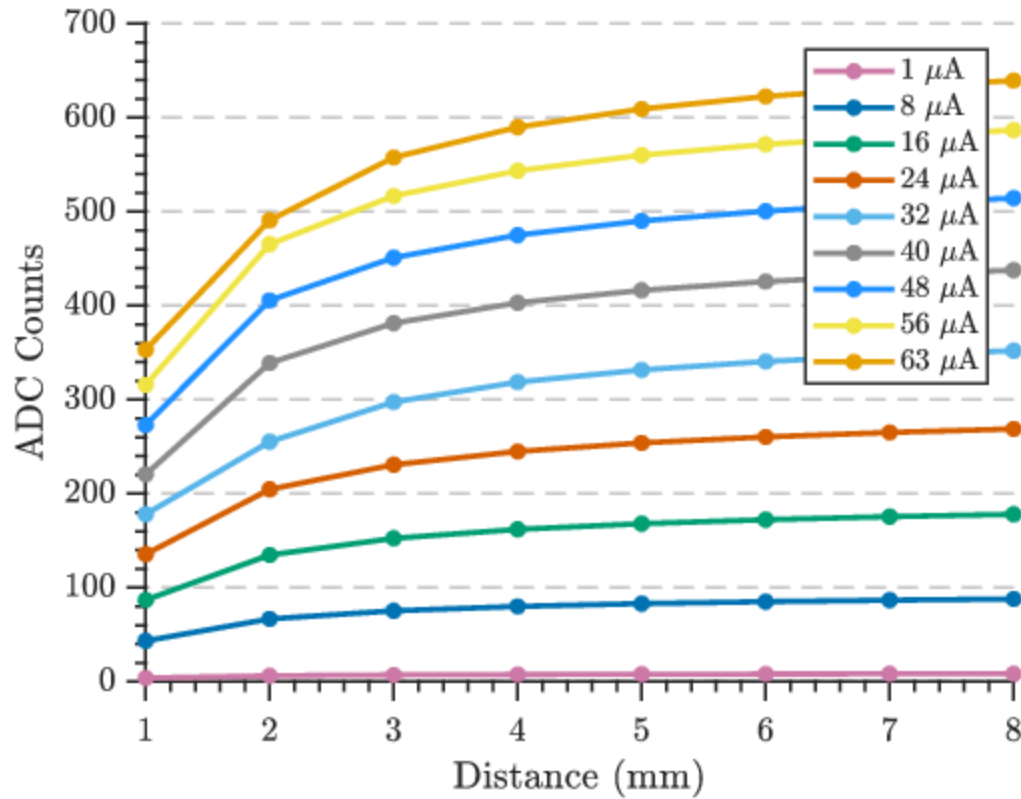
Figure 3.3 Plot of the ADC counts of MPR121 board using different charging currents to analyze operating range.

Similarly, using the same 5x5 cm^2 copper plate, the effect of increasing the charge time was investigated. The MPR121 board only allows charge time to be set to values of 2^n μs, where n is an integer. During these tests, the charging current was kept at 1 μA to ensure only charge time was responsible for saturating the ADC. The results of this test are shown in **Figure 3.4**.
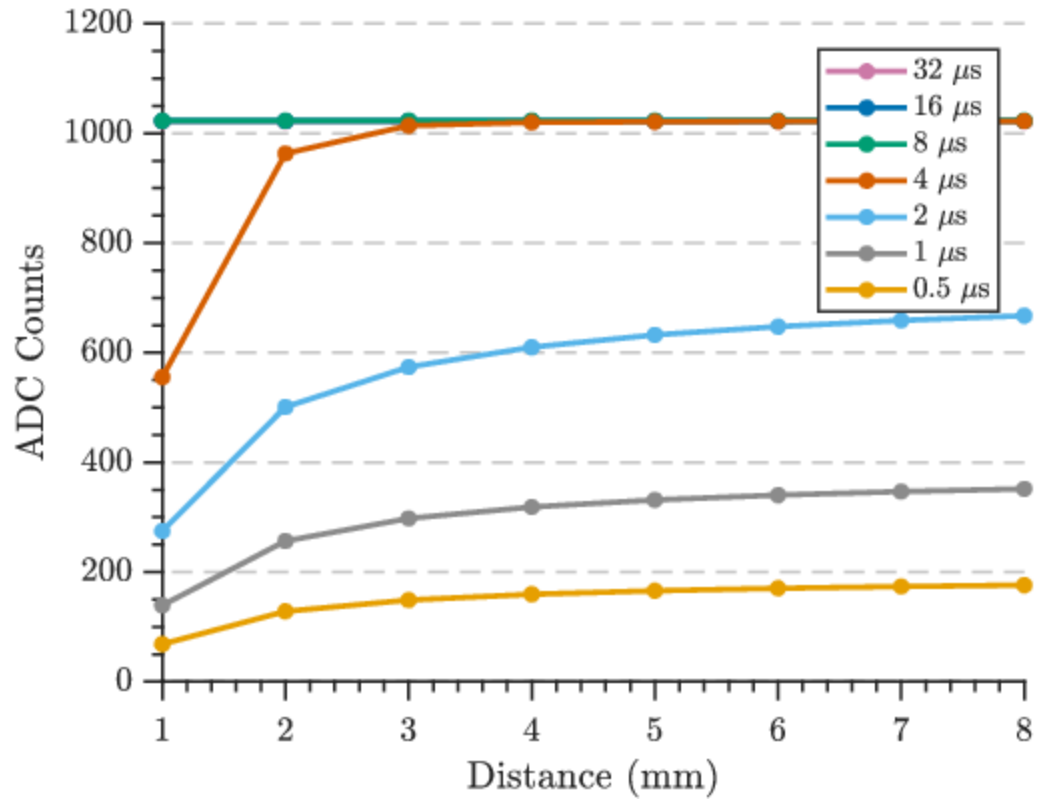
Figure 3.4 Plot of the ADC counts of MPR121 board using different charge time to analyze operating range.

Using the data from the previous tests, six different combinations were tested to determine the configuration that yielded the largest range of ADC counts without saturating the electrode signal. The results of the test are shown in **Figure 3.5** where it is evident that for a charge time of 2 µs and a charging current of 24 µA, the expected range of ADC values will span over a distance of 8 mm without saturating. The motion of a patient is to be expected in the range 0-15 mm, and thus this combination of values allows for the capacitance signal to avoid saturation over this range.

45
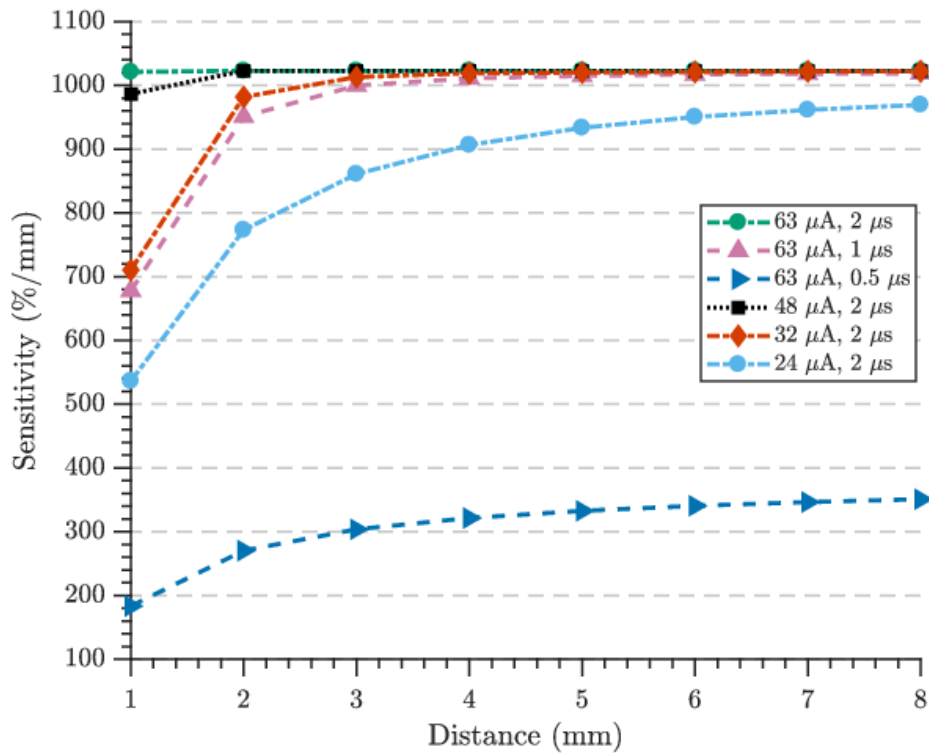
Figure 3.5 Plot of the ADC counts of MPR121 board using different charge time and charging current to select combination that provide the largest operating range.

3.2.3 MPR 121 Filtering

The MPR 121 board acquires the raw data signal and applies a set of three filters to minimize background effects in capacitance measurements. These filters are in place for the benefit of determining whether an electrode is being touched. Touch detection in the MPR121 board depends on absolute capacitance thresholds. If the capacitance is below the threshold, no touch status is registered. Once the threshold is exceeded the MPR121 board registers a touch status. The first filter performs a running average and can be configured

to reduce or increase the number of samples used for the filter. The second filter performs a second average of the data from the first filter and stores the immediate capacitance of the electrodes. Finally, the third filter is used as the baseline value representing the capacitance variation over the long term and slow environment change such as atmospheric moisture and dirt for touch detection.

The first two filters are necessary for the correct operation of the board and do not affect the proximity detection capabilities of the board. However, the third filter presents an obstacle when using proximity detection. This filter changes the baseline as the signal collection is underway and takes this into account when determining if a touch status is detected. The baseline filter performs a check based on noise half delta values, noise count limit and max half delta values set in the register of the MPR121 board. The max half delta determines the largest magnitude of variation in the signal, the noise half delta determines the incremental change when non-noise drift is detected and the noise count limit determines the number of samples consecutively greater than the max half delta necessary before it can be determined that it is non-noise. Based on the magnitude of the signal and duration, the MPR121 board determines if the baseline needs to be adjusted or if it can dismiss the signal as noise. For long enough data collection tests, a baseline change can occur even when the background conditions remain the same. For example, if the proximity of an object is measured in steps and the acquisition time is long enough, the baseline filter will correct the capacitance data and provide a relative baseline that depends on the proximity of the object, not the background conditions. To overcome this, data were obtained from the second filter at all times thus ignoring the corrected baseline reading.

47

3.2.4 National Instruments USB-8452

To communicate with MPR121 board an I2C-to-USB interface device was used. The NI USB-8452 supplies a voltage of 5 V to the MPR121 for the operating voltage. While there is a supply of 5 V, the MPR121 board can accept 5 V but only uses a maximum of 3.6 V. The digital signal output by the MPR121 board is read by the I2C interface and sent via USB to the collection software. The NI USB-8452 acquisition was controlled using a Graphical User Interface (GUI) created in MATLAB. This GUI was also used to unify the acquisition system and the 6-D translation stage.

3.3 DETECTOR PLATE DESIGN

There were several considerations for the design of the detector plate. However, according to the literature (76), a simple shape will perform better in button operations which in principle are similar to proximity detectors, where the measured capacitance depends on the proximity of the object to the detector to determine if a an action will be executed. A circle, a triangle and square shapes were chosen to determine the variability in sensitivities between simple shapes.

The detector plate material considerations included those materials with high conductivity such as gold and silver. However, these materials have a high atomic number which when placed in the path of the treatment beam can affect the dose distribution of the treatment. Therefore, a viable candidate material was copper, with a conductivity of 5.96 x 10^7 S/m and a second material with lower conductivity and lower atomic number such as aluminized Mylar with a conductivity of 3.5 x 10^7 S/m was used to determine the effect of

conductivity in in the signal acquired. When using copper detector plates, three different thicknesses (0.0762 mm, 0.127 mm and 0.254 mm) were tested to determine the best sensitivity.

The detector plate was connected to the MPR121 board with a 25 AWG, 316 UL style coaxial cable (AlphaWire, Elizabeth, NJ). In the case of copper, the coaxial cable was soldered to the detector plate for all but one experiment. To compare aluminized Mylar and copper detector plates, soldering was replaced by the use of silver epoxy (MG Chemicals, Burlington, ON). The coaxial cables were connected at one corner of the detector plate. This was done to allow detector plate placement such that the resulting uneven surface did not interfere with the flatness of the detector plate.

3.4 EXPERIMENTAL SETUP

The variation in sensitivity was investigated with regard to: (i) the shape of the plate, (ii) the dimensions and thickness of the plate and (iii) the material of the plate. This was carried out using a parallel plate setup. This setup consisted of a detector plate with a specific set of variables depending on the test and an opposing conductive plate with an area of 15x15 cm^2 of copper of 0.127 mm thickness. The parallel plate setup was chosen to investigate the best case scenario in sensitivity. This setup was used as a reference point for further experiments such as the volunteer study. The physics of the parallel plate setup are well understood and as opposed to a realistic phantom or human studies, it isolates the effects of detector design from, e.g., variability in the anatomy of human subject.

49

Using a Hexapod translation stage, the detector plate was translated over a range of 15 mm while acquiring data. The Hexapod is a 6-axis positioning system that allows high precision and high repeatability translations. The use of a Hexapod allows for the simulation of sub-millimetre motion that can be experienced by a patient during treatment. These experiments rely on the high accuracy of motions from the translation stage. The Hexapod has a travel range of 50 mm in the X and Y directions and 25 mm in the Z direction. This range is useful to investigate the maximum operating range of the detector plate. Furthermore, the Hexapod has a repeatability of ± 2 µm. The GUI created for this work allowed for automation of motion required for the Hexapod, where the user inputs the desired change in distance and the duration of motion. This in turn starts the data collection process and stores all the relevant information such as Hexapod position and time, ADC counts and capacitance in a single file. The data obtained from the NI USB-8452 was sampled at a rate of 200 Hz. The NI USB-8452 collects data for all electrodes regardless of whether they are being used for data acquisition. This limits the acquisition frequency to 200 Hz.

3.4.1 Plate Shape

Detector plates of different shapes may be desirable when designing an array of individual elements. For example, an array of hexagonal detector plates could be used to create a close-packed, multi-element array, or a linear arrangement of interlocking chevron-shaped detector plates could provide spatial discrimination along one axis. The shapes tested were a circle, a square and a triangle made out of copper with a constant

thickness of 0.127 mm. This thickness was chosen because at the time of testing, there was no data indicating the effects of thickness in sensitivity. Therefore, out of the available three thicknesses, 0.127 mm provided a mid-point of reference. For each shape, the plate area was approximately constant at approximately 25 cm^2. The detector was placed against the L-shaped bracket using double sided tape to ensure that the detector was flat against the surface. A shielded coaxial cable was used to minimize any contributions to capacitance from external sources. A coaxial cable consists of two conductors separated by an insulator. Coaxial cables have a known capacitance, typically in the range of 100 pF/m. This known, constant capacitance can be rejected from measurements of capacitance of a circuit. Using an unshielded wire for electrical connections results in additional unknown capacitance that cannot be dismissed from the circuit. The shielded coaxial cable was soldered to the detector using tin solder.

Using the Hexapod translation stage the detector plate was translated in 1 mm increments every 3 seconds over a range of 15 mm while acquiring data. A total of 11,491 data points were collected. An average of the data was performed at every 1 mm translation. This was repeated for each plate shape. The detector plate initial position was determined through electrical contact with the grounded plate in order to standardize the point of zero plate separation. Any curvature present in the detector or the opposing grounded plate can affect the sensitivity measured. To mitigate this problem every test used new double sided tape to ensure maximum adhesion and no plate remained attached to the L-shaped bracket for more than 2 hours. A level was used to ensure flatness along the detector plate.

When analyzing the data obtained from this setup, data acquired at the initial plate position, i.e., when the detector is making electrical contact with the opposing plate, are ignored. This is due to the fact that when the detector is grounded, the signal measured is not relevant to our experiments. A grounded detector measures an infinite capacitance; after the detector is displaced 1 mm the capacitance drops to measurable values. When the detector is grounded the MPR121 registers 0 ADC counts, at 1 mm separation the signal rapidly increases. Using equation (8) the capacitance at 0 ADC counts is infinite as expected, and when the ADC counts change from grounded to ungrounded there is a large change in signal. This large change results in an artificially high sensitivity arising from equation (9). Therefore all sensitivity data start at distance of 1 mm from the opposing plate. It is important to note that a typical thermoplastic mask is approximately 2-4 mm thick and therefore any sensitivity measurements made in later experiments have a starting point at 4 mm regardless of the presence of a thermoplastic mask.

3.4.2 Plate dimensions

The detector dimensions must be adequate to provide sub-millimetre sensitivity, and the thickness of detector plate must be low enough to limit attenuation of a therapeutic photon beam. The effect of plate dimensions on sensitivity was investigated using copper plates of three different thicknesses (0.0762 mm, 0.127 mm and 0.254 mm), and six different areas (1x1 cm^2, 2x2 cm^2, 3x3 cm^2, 4x4 cm^2, 5x5 cm^2 and, 10x10 cm^2). Each copper plate was displaced in 1 mm increments every 3 seconds over a range of 20 mm.

Three trials were performed for each plate; for each trial, variation of capacitance and sensitivity were recorded.

3.4.3 Plate Material

Two materials with different conductivities were tested to investigate possible effect on sensitivity. Copper was selected as the material with highest conductivity and aluminized Mylar was used for its lower conductivity. Three plate areas ($3x3$ cm^2, $4x4$ cm^2 and, $5x5$ cm^2) were used for both materials. Aluminized Mylar and the copper plate each had a thickness of 0.127 mm, which should attenuate a 6MV beam by only 0.04 % and less than 0.01 %, respectively. Testing methods were similar to those of sections 3.4.1 Plate Shapeand 3.4.2 Plate dimensionswith displacements of 1 mm over a range of 20 mm.

3.4.4 Stability in the linear accelerator environment

To determine the stability of the proposed system during treatment in the linac suite, data were first acquired under controlled laboratory conditions (e.g., no radiofrequency or ionizing radiation interference) with the parallel-plate setup, using a $5x5$ cm^2 copper detector. The opposing grounded plate was placed at a distance of 30 cm to minimize contributions from motion and isolate contributions from RF and ionizing radiation interference. Data were acquired for 3 minutes in a setting with no radiofrequency or ionizing radiation interference. As a worst-case scenario, this was subsequently repeated inside the treatment room with a 6 MV flattening filter-free $10x10$ cm^2 field directed at the copper plate with a 1400 MU/min dose rate. Data sets were compared to assess for possible interference by the linear accelerator or x-ray the photon beam.

53

3.5 VOLUNTEER STUDY

An experiment with a volunteer was performed as a proof-of-concept study and to examine the sensitivity of the proposed system when the conductive plate was displaced by known translations. The conductive plate was placed in an L-shaped bracket attached to the Hexapod (**Figure 3.6**). The plate was then connected to the MPR 121 chip and data were acquired at a sampling rate of 200 Hz. The Hexapod was used to displace the conductive plate away from the volunteer in 1 mm steps every 3 seconds.

A thermoplastic mask, identical to that used for cranial SRS patients (Brainlab AG) was fitted to the volunteer, who was placed in the couch mount to simulate the patient position during treatment. A second test setup was used to determine the effect of placing the thermoplastic mask between the detector and the volunteer.

Given that future development will involve an array of detectors at various locations around the cranium, three anatomical sites were tested: the vertex of the cranium, temple and forehead (shown in **Figure 3.6**). Tests to determine the effect of the thermoplastic mask were only done for sites near the temple and the forehead. During the test without a thermoplastic mask the volunteer's cranium was resting on the occipital portion of the mask. This setup maintained a stable initial position to use for comparison. The vertex of the cranium did not require two tests because the thermoplastic mask does not cover this site. Depending on which site is to be monitored, the Hexapod was positioned such that the plate was approximately parallel to the tangent to the patient surface. To standardize an initial point of reference, i.e., to set the nominal point of zero separation between the detector and cranium, a grounded piece of aluminized Mylar was placed on

top of each site to determine when the detector plate had made electrical contact. **Figure 3.6** shows the setup used for acquiring data when the conductive plate is positioned above the volunteer's forehead.

In section 1.3.1 Patient Motion during SRSwhere intrafraction motion during SRS treatments is discussed, it was stated that the fidelity of a patient's initial position with respect to a planning CT can degrade as treatment time increases. In this experiment it is assumed that the volunteer does not move inside the mask.
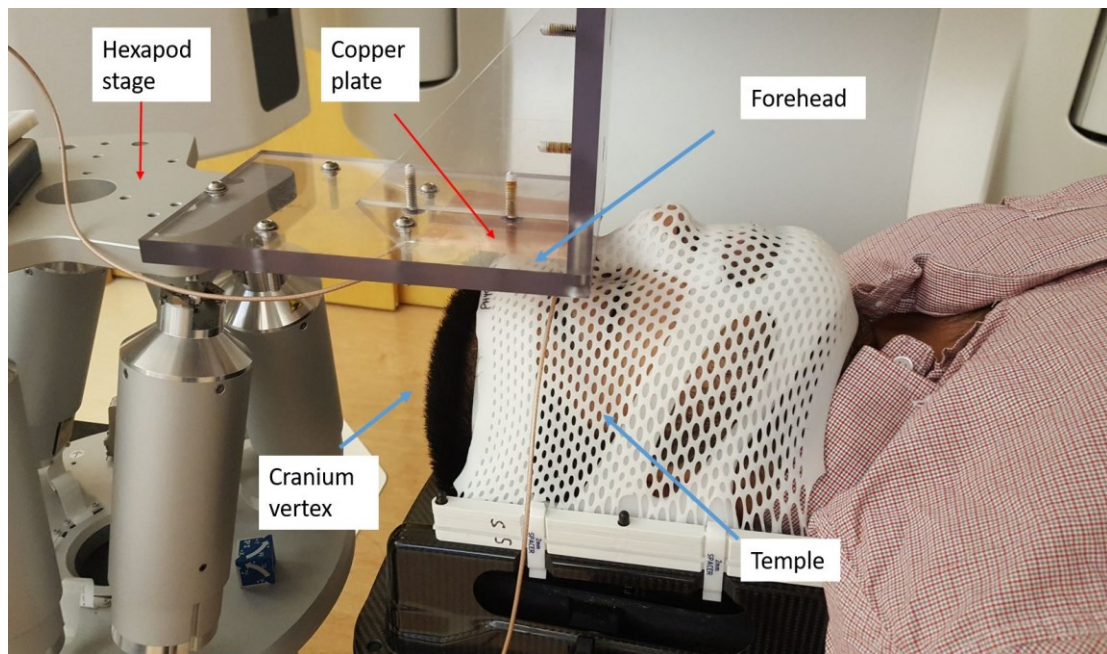
Figure 3.6 Experimental setup of volunteer used to measure differences in sensitivity. Sites tested are shown with a blue arrow.

A 9x9 cm^2 copper detector with a 0.127 mm thickness was used for the cranium vertex and for the site near the temple. This plate detector dimension was chosen based on data acquired during plate dimension tests.

CHAPTER 4 RESULTS AND DISCUSSION

4.1 PLATE SHAPE

Figure 4.1 shows the variation of sensitivity when using conductive plates of different shapes. This demonstrates that for plates that have a similar area, sensitivity is similar. This agrees with equation (5) where capacitance is directly proportional to the area.
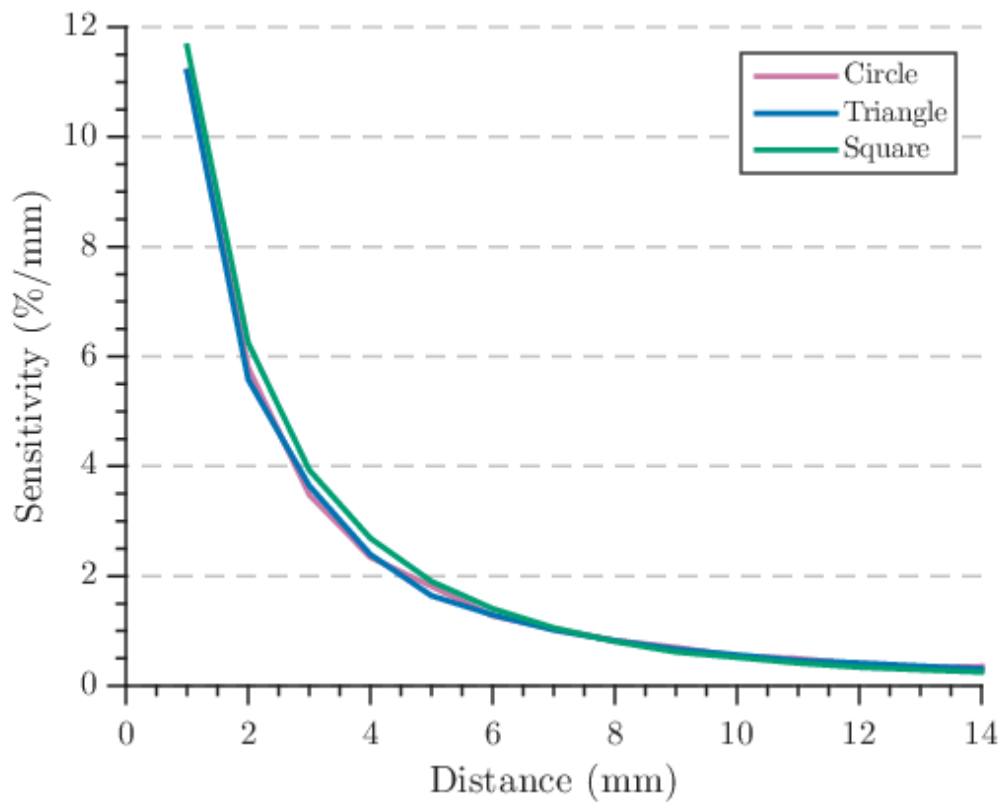
Figure 4.1 Sensitivity for a parallel plate setup with the detector plate shape area of 25 cm².

Over the range examined, sensitivity varies between 0.5 %/mm and 11.5 %/mm for all three plates. The maximum variation in sensitivity between shapes was of 0.45 %/mm

for distances smaller than 6 mm. This variation was not systematic, however the square shape shows a slightly higher sensitivity for a range between 1 and 6 mm. When the detector separation is 6 mm or greater, the variation in sensitivity between plate shapes decreases to below 0.03 %/mm

4.2 PLATE SIZE

Plate size and thickness has a significant impact on capacitance, making it an important variable in determining sensitivity. **Figure 4.3** highlights the difference in sensitivities between plate thicknesses of 0.0762 mm, 0.127 mm and 0.254 mm, and dimensions ranging from 1x1 cm^2 to a 10x10 cm^2. Increasing the plate area directly increases the sensitivity of the detector, but variation with thickness was comparatively low. Figure 4.2 compares the differences in sensitivity for detector thicknesses of 0.0762

mm and 0.254 mm for three detector sizes.
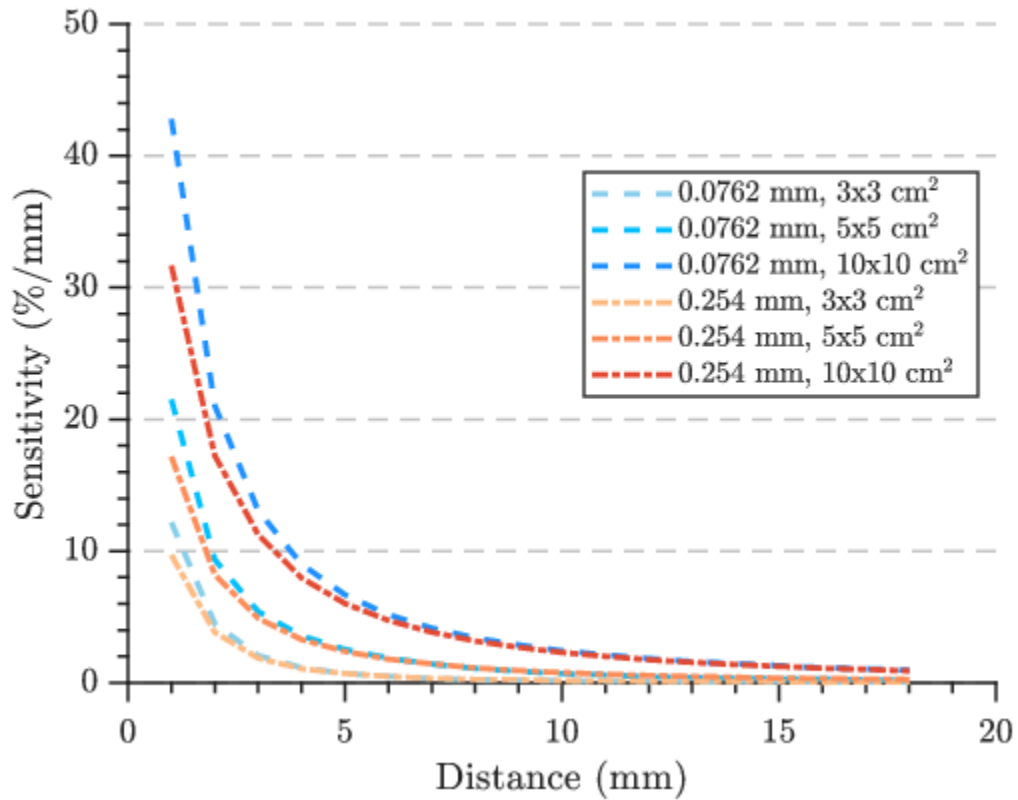
Figure 4.2 Sensitivity comparison of detector thicknesses of 0.0762 mm and 0.254 mm.

A decrease in sensitivity was observed in detector plates with the same area. At a distance of 4 mm away from the grounded plate, for example, the sensitivity of the detector increases as the thickness decreases. Using a 10x10 cm^2 detector the sensitivities at 4 mm were found to be 9 %/mm, 8.85 %/mm and 7.95 %/mm for 0.0762 mm, 0.127 mm and 0.254 mm plates, respectively. At a distance of 15 mm, the sensitivities for the three plates are 1.3 %/mm, 1.26 %/mm and 1.24 %/ mm, respectively.
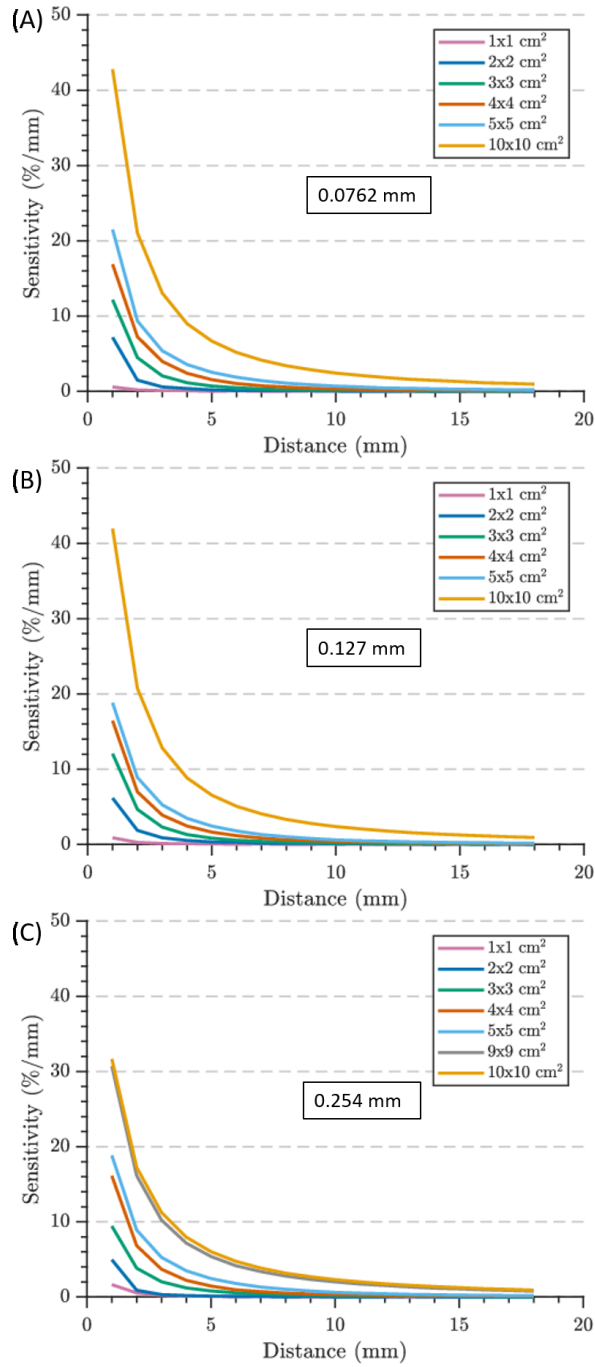
Figure 4.3 (A) Sensitivity of a copper plate detector of thickness 0.0762 mm. (B) Sensitivity of a copper plate detector of thickness 0.127 mm. (C) Sensitivity of a copper plate detector of thickness 0.254 mm.

4.3 PLATE MATERIAL

Figure 4.4 shows a comparison of copper and aluminized Mylar detector plates for three different plate dimensions. For similar areas, the sensitivity of a copper plate is approximately 8 % higher at distances shorter than 6 mm however, as the plate separation is increased, the sensitivity difference is diminished; beyond 6 mm, the two materials show sensitivities within 1% of each other.
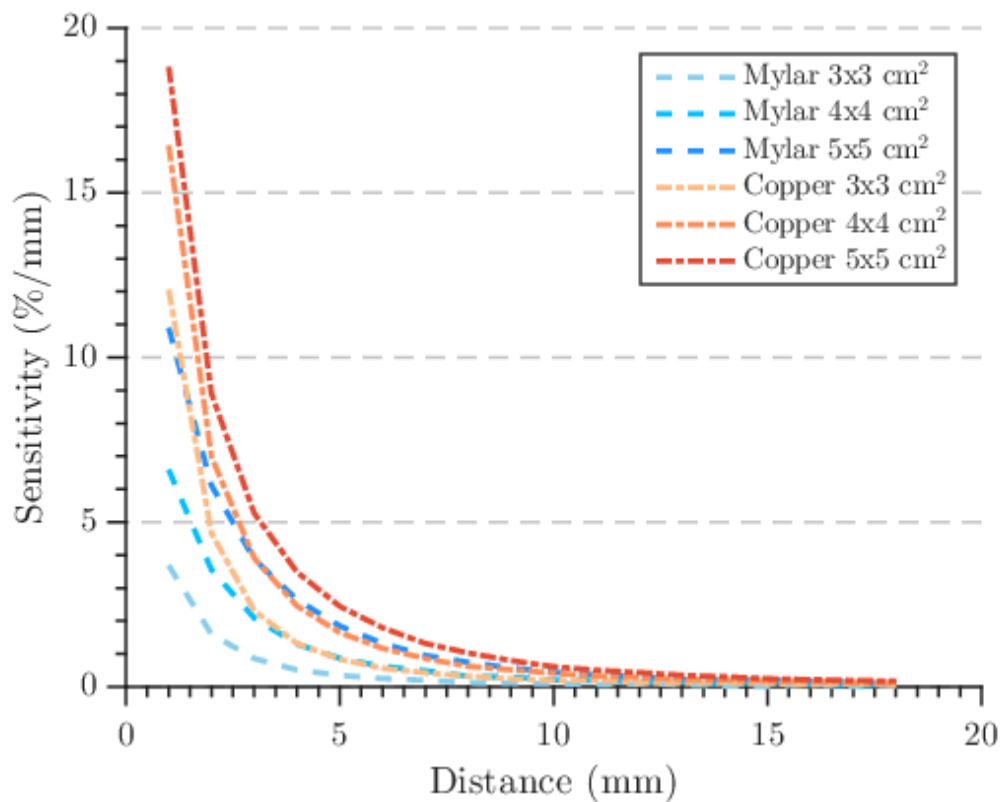
Figure 4.4 Sensitivity comparison between copper and aluminized Mylar plates of varying areas.

4.4 STABILITY

     Figure 4.5A demonstrates a probability histogram for the data acquired during a

three minute test in a laboratory environment. The average signal for both systems was

842 with a standard deviation of 1.16 for the controlled environment setup and 1.19 for

treatment room setup with an incident beam on the detector. Comparing this to **Figure**

4.5B, when the treatment beam is incident on the detector, there is no apparent effect on

the stability of the signal. These results indicate that the system is viable for use in the

treatment room during delivery of a megavoltage photon beam without compromising the

stability of the signal.
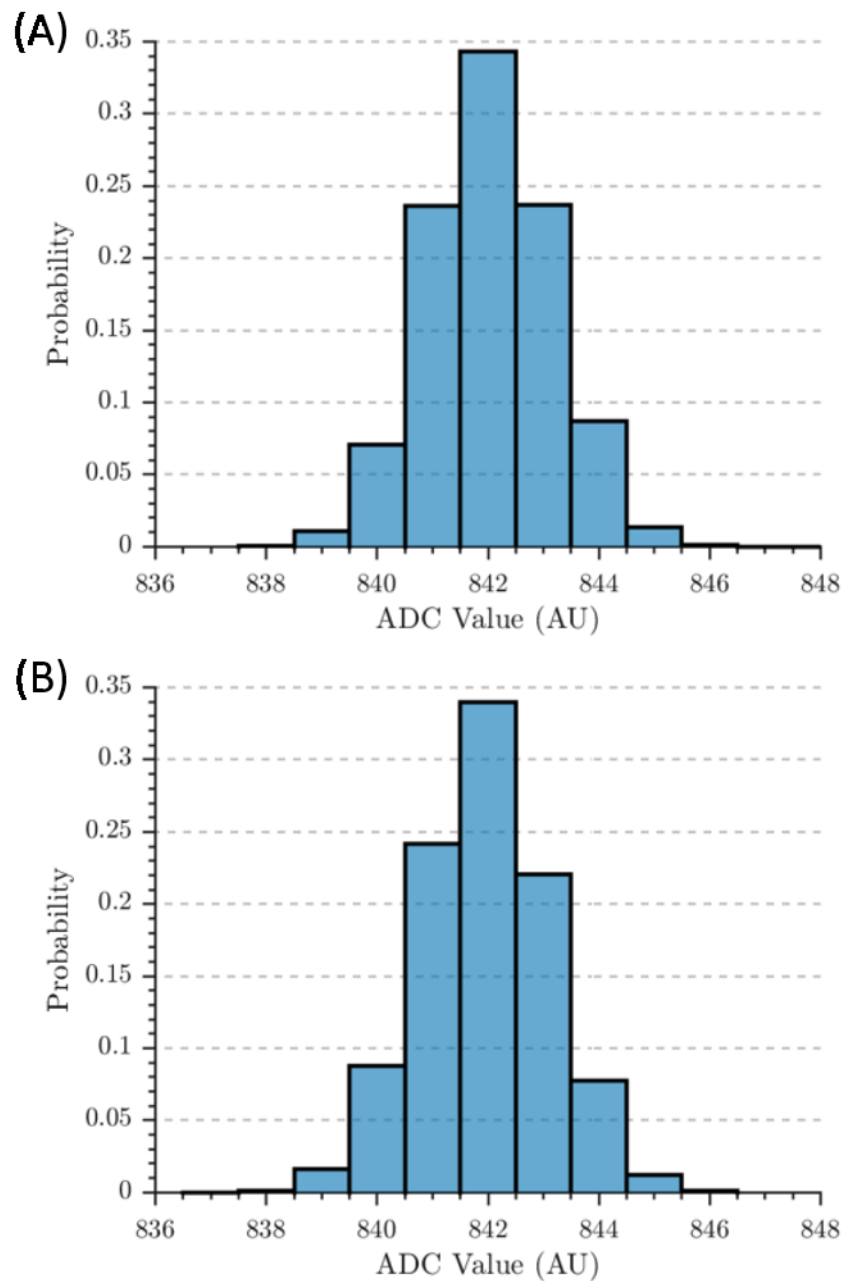
Figure 4.5 Relative probability of signal values of the detector with (A) no beam in a controlled environment and (B) with a 6 MV, 1400 MU/min, 10x10 cm2 photon beam incident on the detector plate.

4.5 VOLUNTEER STUDY

Figure 4.6 shows the sensitivity of a copper plate with area 9x9 cm^2 and thickness
of 0.127 mm, for the vertex of the volunteer's cranium. Values agree approximately with
the results from 0 in terms of sensitivity. A total of 10,474 data points were acquired
during the 52 second acquisition.
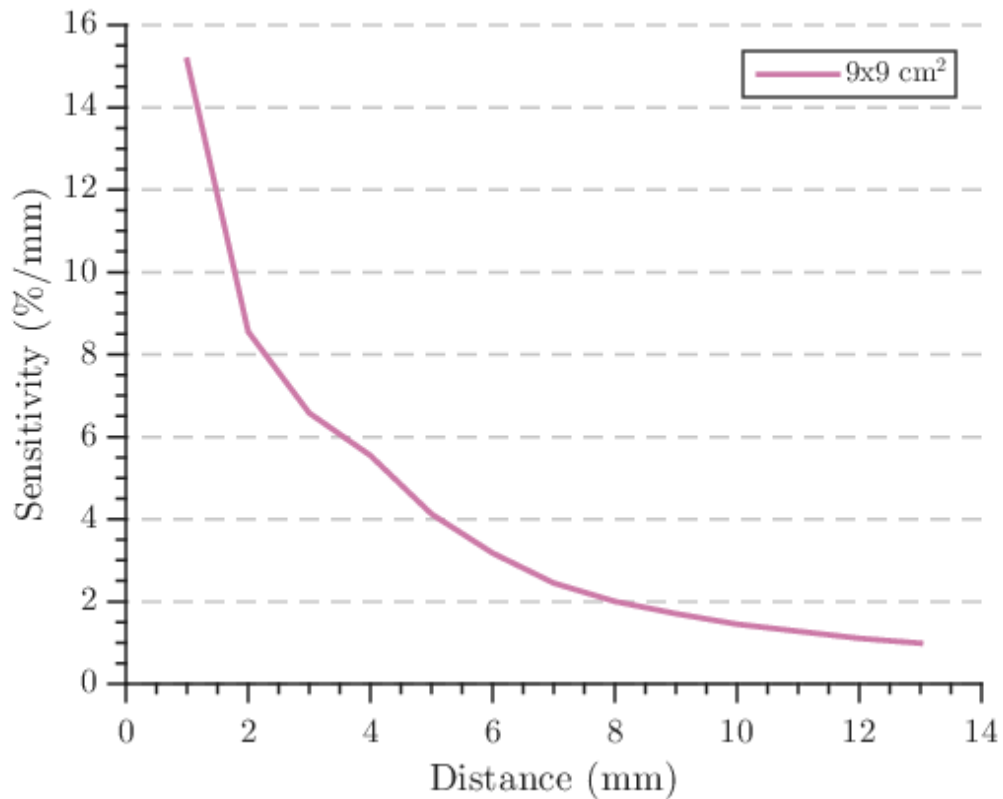
**Figure 4.6 Sensitivity of a 9x9 cm^2 detector plate when displaced up to 14 mm away from
the volunteer's cranial vertex.**

The cranial vertex was not covered by the thermoplastic mask, and therefore the
effect of the mask was investigated using the two remaining test sites. **Figure 4.7** shows
the effect of the thermoplastic on sensitivity compared to that of the volunteer's forehead

without the mask. The thermoplastic mask has a thickness of 4 mm. To standardize

measurements with and without the thermoplastic mask, the distance measurement was

relative to the skin for both the mask-on and mask-off cases. At this site, a detector plate

of 9x9 cm^2 was used. When the thermoplastic mask is between the detector and the

cranium, an increase in sensitivity of 0.02 % was realized.
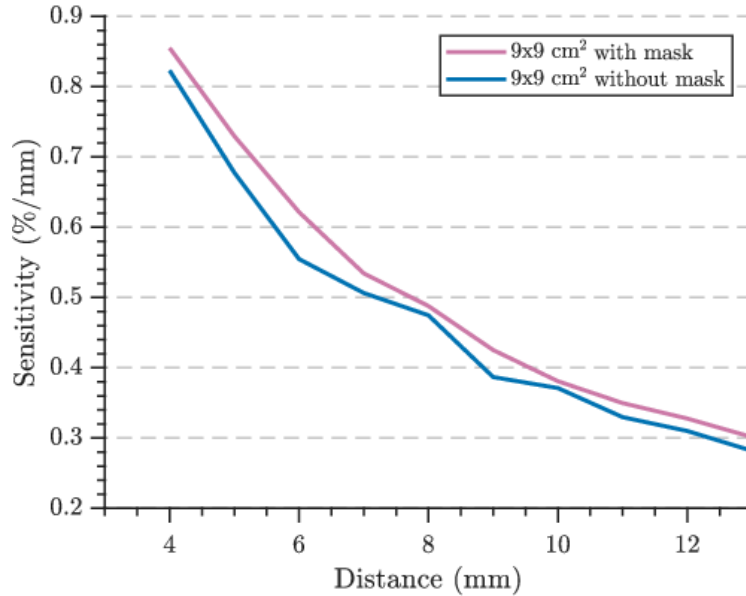
Figure 4.7 (A) Sensitivity of a 9x9 cm^2 copper plate detector when placed above the volunteer's forehead.

    Figure 4.7 shows the effect of the thermoplastic mask when the detector is placed

near the volunteer's temple. Overall the effect of having a thermoplastic mask between

detector and cranium increases the signal measured and therefore the sensitivity. In this

case the sensitivity increase can be attributed to the higher relative permittivity of the

thermoplastic material (~2.25) compared to that of air, i.e., it is likely that the mask is

acting as a more effective dielectric material. The large differences in relative

permittivity between the thermoplastic mask and the patient, results only in motion detection from the patient and not the mask. If the relative permittivity of the mask was comparable to that of the patient, the detector would then detect the mask and patient as a single object rather than a dielectric, making motion detection from the patient less effective.

4.6 DISCUSSION

In this study we have examined several key physical parameters of a capacitive position detector, allowing for an informed selection in the design of a system for monitoring patient intra-fraction cranial motion. The proposed detector plate was also tested in a mock clinical setting with a volunteer inside a thermoplastic mask, replicating the patient setup while performing SRS treatments. As illustrated in **Figure 4.5** the stability of the system shows that the signal acquired from the detector experiences little to no variability within the treatment setting.

Results from Figure 4.1 show that the difference between shapes is largest at shorter distances from the object to be measured. A square detector was used in this study because it showed a higher sensitivity. This can be attributed to a more accurate estimation of the area when creating the detector plates.

Results from **Figure 4.3** indicate that a thin detector plate can perform just as effectively as a thicker plate, fortuitously resulting in less perturbation the treatment beam. Additionally, the area of the detector can be increased to improve the sensitivity of the system. Therefore, if the proposed system has a low sensitivity a simple solution

would be to increase the area of the detectors. The likely tradeoff is spatial resolution; however this will be examined in forthcoming work using a multi-detector array.

This study shows that a material with a higher conductivity will allow greater sensitivity when comparing detectors of same size. A material with higher conductivity such as silver could be used to improve sensitivity of the detectors. This is inferred based on the results from section 3.4.3, where copper, with a higher conductivity than Mylar, showed a higher sensitivity for similar detector sizes. According to the derivation of equation (3) in section 2.2 conductivity and resistivity have no effect on capacitance given that the charges in the conductors distribute themselves evenly over the plates in a short period of time (77). This results in no current and no voltage drop. However, during the charge cycle of the detector, the charges in a high conductivity plate will be distributed more quickly. If the charge cycle is short enough, the charges won't be evenly distributed, therefore the electric field lines will only cover a portion of the low conductivity plate while they cover a larger portion of the high conductivity plate.

During the volunteer study a 9x9 cm^2 detector plate was used to measure the sensitivity of the system within a clinical setup. This detector size was chosen because as shown in section 4.2, a larger detector area results in higher sensitivity. While the results for the cranium vertex show a sensitivity of 11 %/mm, the detector size choice was not optimal for the forehead. In our current testing setup, the placement of the detector covered the volunteer's forehead but the large area resulted in a portion of the detector measuring capacitance above the forehead to the top of the cranium. This resulted in a lower average capacitance and therefore a lower sensitivity. It is important to note that

66

head displacements have been shown to have tethering effects of brain–skull connections (78). This allowed to make the assumption that detection of motion of the cranium relates to motion of structures inside the cranium.

During testing, data were acquired continuously. Every 1 mm, data were acquired for 3 seconds and the average capacitance was used. Given the high temporal resolution of the system it is possible to decrease the time average and use finer resolutions for a better determination of sensitivities of real-time motions. A longer temporal sample allows for data averaging at the expense of temporal resolution. Furthermore, changing the magnitude of the displacements to smaller values will provide a more accurate estimate of how accurate the sub-millimetre detection of the system is.

As demonstrated by the volunteer study it is possible to detect cranial motions while a patient is within the thermoplastic mask. The system shows a sensitivity of 1 %/mm at a distance of 12 mm from the volunteer's cranium vertex. With a coefficient of variation of only 0.14 % it is possible to accurately detect sub-millimetre motions even at this distance, making this detector viable for patient tracking.

The advantages of capacitive monitoring include a stable real-time monitoring system that can be used during treatment without perturbation of the acquired signal. The system is completely passive. The approach does not incur in additional dose to the patient and it is non-invasive. The temporal resolution of readout is much higher than likely needed during guidance of SRS and SRT, allowing for some averaging of noise if required.

The data presented here applies to a single detector but can be used as a guide in development of an array providing 3D positional information.

67

A detector plate with dimensions larger than the site to be monitored will average capacitance measured resulting in a loss in spatial resolution but for large sites such as the cranium vertex can provide a better sensitivity. For smaller sites, a smaller detector will provide a better spatial resolution that does not average over regions that are not of interest.

The ideal position of a detector is as close as possible to the patient's skin to take advantage of the high sensitivity of the system. This in practice is not possible at all sites due to the thermoplastic mask immobilization. Placing a detector further away from the patient will result in a loss in sensitivity.

This system provides advantages over the systems mentioned in section 1.3.2 Patient Position Monitoring for SRSHowever, it also has some limitations. In its current state, the system has to be placed in close proximity to the patient without interfering with the immobilization system for accurate measurements. The measurement of capacitance depends on the relative permittivity of materials between the detector and the volunteer. The volunteer tested had short hair which allowed for a closer measurement to the skin. The effect of environmental variables, e.g., presence of sweat and a fuller set of hair, must be investigated to determine how sensitivity changes in different patient scenarios.

CHAPTER 5 CONCLUSIONS

5.1 SUMMARY OF WORK

In this study, we investigated the variability of sensitivity on various design parameters of a capacitive detector plate and demonstrated the feasibility of near real-time position detection during a mock clinical setup with a volunteer inside a thermoplastic mask.

Design parameters included detector size, shape and material. A key variable in detector sensitivity is plate dimension, where increasing the area of a plate from 5x5 cm^2 to 10x10 cm^2 causes an increase of sensitivity by 10 %/mm at minimum. The stability of the detector in our current setting was excellent and unaffected by the linear accelerator and administration of a photon beam at high dose rate, with a coefficient of variation (standard deviation over mean) of 0.14 %. However, this does not represent all clinical scenarios. Further tests are required to investigate the effect of a photon beam at high dose rate when an opposing grounded plate is placed in close proximity. The stability measured here should be adequate to allow sub-millimetre sensitivity at detector distances larger than 15 mm with the designs tested here.

The volunteer study confirmed that motions can be detected with the proposed detector design at various locations around the cranium, with, or without a thermoplastic mask. When a 9x9 cm^2 detector is placed at the cranium's vertex the sensitivity of the detector at 13 mm is 1 %/mm. This sensitivity is comparably smaller than that of a 10x10 cm^2 detector, this can be attributed to the differences in shape from a flat opposing plate to a curved surface where the distance from the surface to the detector is not uniform.

69

However, this sensitivity allows for the detection of sub-millimetre motions given the stability and variability of the system. When the detector is placed at the forehead, the sensitivity increases potentially due to the presence of the thermoplastic mask acting as a dielectric.

The proposed detector demonstrates the usefulness of capacitance when used to detect motions inside a thermoplastic mask used for frameless stereotaxy. The proposed detector is capable of detecting sub-millimetre motions over a distance of 15 mm. Furthermore, this detector does not incur any additional dose to the patient and can be used continuously during treatment providing real-time motion tracking of the cranium.

5.2 FUTURE WORK

This study focused on the optimization of the design of a single detector plate for capacitance motion detection. Creating an array of detectors using the information provided is the next step in creating a capacitance monitoring system. The design and impact on sensitivity of multiple detector plates in close proximity must be investigated. A method of calibration for the array is a vital step required for proper monitoring of position during treatment. Further research into capacitive monitoring will make the implementation of this technology in a clinical setting increasingly feasible.

BIBLIOGRAPHY

1. Canadian Cancer Society's Advisory Comittee on Cancer Statistics. Canadian Cancer Statistics 2017 [Internet]. www.cancer.ca. [cited 2017 Jul 18]. Available from: cancer.ca/Canadian-CancerStatistics-2017-EN.pdf

2. NIH Categorical Spending -NIH Research Portfolio Online Reporting Tools (RePORT) [Internet]. [cited 2017 Jul 17]. Available from: https://report.nih.gov/categorical_spending.aspx

3. Hu Q, Sun W, Wang C, Gu Z. Recent advances of cocktail chemotherapy by combination drug delivery systems. Adv Drug Deliv Rev. 2016 Mar 1;98:19–34.

4. George Miller MacKee. X-rays and radium in the treatment of diseases of the skin [Internet]. Lea & Febiger; 1921. 594 p. Available from: http://archive.org/details/xraysandradiumi00mackgoog

5. Pioneer in X-Ray Therapy. Science. 1957;125(3236):18–9.

6. Chamberlain WE, Young BR. Should the Method of Coutard be Applied in All Cases of Cancer Treated by Roentgen Rays? Radiology. 1937 Aug 1;29(2):186–9.

7. Halperin EC, Perez CA, Brady LW. Perez and Brady's Principles and Practice of Radiation Oncology. Lippincott Williams & Wilkins; 2008. 2152 p.

8. Hayter CRR, Payne D, Ege G. Radiation oncology in Canada 1895–1995. Int J Radiat Oncol. 1996 Sep 1;36(2):487–96.

9. Thwaites DI, Tuohy JB. Back to the future: the history and development of the clinical linear accelerator. Phys Med Biol. 2006;51(13):R343.

10. Chao A. Reviews of Accelerator Science and Technology: Medical applications of accelerators. World Scientific; 2009. 321 p.

11. Podgoršak EB. Radiation Oncology Physics: A Handbook for Teachers and Students. International Atomic Energy Agency; 2005. 704 p.

12. Division for Human Health: DIRAC (DIrectory of RAdiotherapy Centres) [Internet]. [cited 2017 Jul 29]. Available from: https://dirac.iaea.org/Query/Map2?mapId=0

13. PTCOG - Facilities in Operation [Internet]. [cited 2017 Jul 29]. Available from: https://www.ptcog.ch/index.php/facilities-in-operation

14. Khan FM. The Physics of Radiation Therapy. Lippincott Williams & Wilkins; 2010. 576 p.

15. Podgoršak EB, Rawlinson JA, Glavinović MI, Johns HE. Design of x-ray targets for high energy linear accelerators in radiotherapy. Am J Roentgenol. 1974 Aug 1;121(4):873–82.

16. O'Brien PF, Gillies BA, Schwartz M, Young C, Davey P. Radiosurgery with unflattened 6-MV photon beams. Med Phys. 1991 May 1;18(3):519–21.

17. Georg D, Knöös T, McClean B. Current status and future perspective of flattening filter free photon beams. Med Phys. 2011 Mar 1;38(3):1280–93.

18. Dyk JV, Dyk JV. The Modern Technology of Radiation Oncology: A Compendium for Medical Physicists and Radiation Oncologists. Medical Physics Pub.; 1999. 1104 p.

19. Sahgal A, Lo SS, Ma L, Sheehan JP. Image-Guided Hypofractionated Stereotactic Radiosurgery: A Practical Approach to Guide Treatment of Brain and Spine Tumors. CRC Press; 2016. 368 p.

20. Mell LK, Mehrotra AK, Mundt AJ. Intensity-modulated radiation therapy use in the U.S., 2004. Cancer. 2005 Sep 15;104(6):1296–303.

21. Otto K. Volumetric modulated arc therapy: IMRT in a single gantry arc. Med Phys. 2008 Jan 1;35(1):310–7.

22. Holt A, Gestel DV, Arends MP, Korevaar EW, Schuring D, Kunze-Busch MC, et al. Multi-institutional comparison of volumetric modulated arc therapy vs. intensity-modulated radiation therapy for head-and-neck cancer: a planning study. Radiat Oncol. 2013 Jan 31;8(1):26.

23. Gamma Knife Radiosurgery [Internet]. Pietro Mortini. [cited 2017 Jul 31]. Available from: http://www.pietromortini.com/gamma-knife-radiosurgery/

24. About Gamma Knife Radiosurgery [Internet]. Dr. Ravi- Gamma Knife Surgeon Malaysia. 2017 [cited 2017 Jul 31]. Available from: https://www.gammaknifedoctor.com/about-us/about-gamma-knife-radiosurgery/

25. Bichay TJ, Mayville A. The Continuous Assessment of Cranial Motion in Thermoplastic Masks During CyberKnife Radiosurgery for Trigeminal Neuralgia. Cureus [Internet]. 2016;8(5). Available from: http://www.ncbi.nlm.nih.gov/pmc/articles/PMC4905702/

26. Robar JL, Clark BG, Schella JW, Kim CS. Analysis of patient repositioning accuracy in precision radiation therapy using automated image fusion. J Appl Clin Med Phys. 2005 Dec 1;6(1):71–83.

27. Minniti G, Scaringi C, Clarke E, Valeriani M, Osti M, Enrici RM. Frameless linac-based stereotactic radiosurgery (SRS) for brain metastases: analysis of patient repositioning using a mask fixation system and clinical outcomes. Radiat Oncol Lond Engl. 2011 Nov 16;6:158.

28. Kang KM, Chai GY, Jeong BK, Ha I-B, Lee S, Park KB, et al. Estimation of optimal margin for intrafraction movements during frameless brain radiosurgery. Med Phys. 2013 May 1;40(5):n/a-n/a.

29. Li G, Ballangrud A, Chan M, Ma R, Beal K, Yamada Y, et al. Clinical experience with two frameless stereotactic radiosurgery (fSRS) systems using optical surface imaging for motion monitoring. J Appl Clin Med Phys Am Coll Med Phys. 2015 Jul 8;16(4):5416.

30. Peng JL, Kahler D, Li JG, Samant S, Yan G, Amdur R, et al. Characterization of a real-time surface image-guided stereotactic positioning system. Med Phys. 2010 Oct 1;37(10):5421–33.

31. Gevaert T, Verellen D, Engels B, Depuydt T, Heuninckx K, Tournel K, et al. Clinical evaluation of a robotic 6-degree of freedom treatment couch for frameless radiosurgery. Int J Radiat Oncol Biol Phys. 2012 May 1;83(1):467–74.

32. Opp D, Feygelman V, Sarangkasiri S, Walker L, Brem S, Chinnaiyan P, et al. Pre-treatment Simulation of Target Motion for Frameless Intracranial Stereotactic Radiosurgery Treatments using the Novalis Exactrac System. Int J Radiat Oncol. 2009 Nov 1;75(3):S602.

33. Ramakrishna N, Rosca F, Friesen S, Tezcanli E, Zygmanszki P, Hacker F. A clinical comparison of patient setup and intra-fraction motion using frame-based radiosurgery versus a frameless image-guided radiosurgery system for intracranial lesions. Radiother Oncol. 2010 Apr 1;95(1):109–15.

34. Clark GM, Popple RA, Young PE, Fiveash JB. Feasibility of Single-Isocenter Volumetric Modulated Arc Radiosurgery for Treatment of Multiple Brain Metastases. Int J Radiat Oncol. 2010 Jan 1;76(1):296–302.

35. Nakamura JL, Verhey LJ, Smith V, Petti PL, Lamborn KR, Larson DA, et al. Dose conformity of gamma knife radiosurgery and risk factors for complications. Int J Radiat Oncol. 2001 Dec 1;51(5):1313–9.

36. Gevaert T, Steenbeke F, Pellegri L, Engels B, Christian N, Hoornaert M-T, et al. Evaluation of a dedicated brain metastases treatment planning optimization for radiosurgery: a new treatment paradigm? Radiat Oncol Lond Engl [Internet]. 2016 Feb 2;11. Available from: http://www.ncbi.nlm.nih.gov/pmc/articles/PMC4736109/

37. Guckenberger M, Roesch J, Baier K, Sweeney RA, Flentje M. Dosimetric consequences of translational and rotational errors in frame-less image-guided radiosurgery. Radiat Oncol. 2012 Apr 24;7(1):63.

38. Ryken TC, Meeks SL, Pennington EC, Hitchon P, Traynelis V, Mayr NA, et al. Initial clinical experience with frameless stereotactic radiosurgery: analysis of accuracy and feasibility. Int J Radiat Oncol. 2001 Nov 15;51(4):1152–8.

39. Chang SD, Main W, Martin DP, Gibbs IC, Heilbrun MP. An Analysis of the Accuracy of the CyberKnife: A Robotic Frameless Stereotactic Radiosurgical System. Neurosurgery. 2003 Jan 1;52(1):140–7.

40. TrueBeam® Radiotherapy System | Varian Medical Systems [Internet]. [cited 2017 Jul 31]. Available from: https://www.varian.com/oncology/products/treatment-delivery/truebeam-radiotherapy-system

41. ExacTrac X-Ray Monitoring [Internet]. Brainlab. [cited 2017 Jul 31]. Available from: https://www.brainlab.com/en/radiosurgery-products/exactrac/

42. John Stoddard Cancer Center Features New Technology to Help Protect Patients' Hearts [Internet]. www.unitypoint.org/. [cited 2017 Jul 31]. Available from: https://www.unitypoint.org/article.aspx?id=666cac5b-45f2-4e03-bb03-d5eec5c5e409

43. Srinivasan K, Mohammadi M, Shepherd J. Applications of linac-mounted kilovoltage Cone-beam Computed Tomography in modern radiation therapy: A review. Pol J Radiol. 2014 Jul 3;79:181–93.

44. Zhu J. Feasibility of using cone-beam CT to verify and reposition the optically guided target localization of linear accelerator based stereotactic radiosurgery. Med Phys. 2011 Jan 1;38(1):390–6.

45. Chang J, Yenice KM, Narayana A, Gutin PH. Accuracy and feasibility of cone-beam computed tomography for stereotactic radiosurgery setup. Med Phys. 2007 Jun 1;34(6Part1):2077–84.

46. Jin J-Y, Ryu S, Faber K, Mikkelsen T, Chen Q, Li S, et al. 2D/3D Image fusion for accurate target localization and evaluation of a mask based stereotactic system in fractionated stereotactic radiotherapy of cranial lesions. Med Phys. 2006 Dec 1;33(12):4557–66.

74

47. Jin J-Y, Yin F-F, Tenn SE, Medin PM, Solberg TD. Use of the BrainLAB ExacTrac X-Ray 6D System in Image-Guided Radiotherapy. Med Dosim. 2008 Jun 1;33(2):124–34.

48. Takakura T, Mizowaki T, Nakata M, Yano S, Fujimoto T, Miyabe Y, et al. The geometric accuracy of frameless stereotactic radiosurgery using a 6D robotic couch system. Phys Med Biol. 2010;55(1):1.

49. Yan H, Yin F-F, Kim JH. A phantom study on the positioning accuracy of the Novalis Body system. Med Phys. 2003 Dec 1;30(12):3052–60.

50. Stevens MTR, Parsons DD, Robar JL. Patient specific methods for room-mounted x-ray imagers for monoscopic/stereoscopic prostate motion monitoring. J Appl Clin Med Phys. 2017 Jul 1;18(4):40–50.

51. Poulsen PR, Cho B, Sawant A, Keall PJ. Implementation of a New Method for Dynamic Multileaf Collimator Tracking of Prostate Motion in Arc Radiotherapy Using a Single kV Imager. Int J Radiat Oncol. 2010 Mar 1;76(3):914–23.

52. Li S, Liu D, Yin G, Zhuang P, Geng J. Real-time 3D-surface-guided head refixation useful for fractionated stereotactic radiotherapy. Med Phys. 2006 Feb 1;33(2):492–503.

53. ClearVision™ & PureVision™ Masks [Internet]. [cited 2017 Jul 31]. Available from: http://civcort.com/ro/thermoplastic/clearvision-purevision-masks/clearvision-purevision-masks21.htm

54. Li G, Ballangrud Å, Kuo LC, Kang H, Kirov A, Lovelock M, et al. Motion monitoring for cranial frameless stereotactic radiosurgery using video-based three-dimensional optical surface imaging. Med Phys. 2011 Jul 1;38(7):3981–94.

55. Bert C, Metheany KG, Doppke K, Chen GTY. A phantom evaluation of a stereo-vision surface imaging system for radiotherapy patient setup. Med Phys. 2005 Sep 1;32(9):2753–62.

56. De Los Santos J, Popple R, Agazaryan N, Bayouth JE, Bissonnette J-P, Bucci MK, et al. Image Guided Radiation Therapy (IGRT) Technologies for Radiation Therapy Localization and Delivery. Int J Radiat Oncol. 2013 Sep 1;87(1):33–45.

57. Franz AM, Schmitt D, Seitel A, Chatrasingh M, Echner G, Oelfke U, et al. Standardized accuracy assessment of the calypso wireless transponder tracking system. Phys Med Biol. 2014;59(22):6797.

58. Kim K i-Hwan, Cho M-J, Kim J-S, Kim J-S, Song C-J, Song S-H, et al. Isocenter accuracy in frameless stereotactic radiotherapy using implanted fiducials. Int J Radiat Oncol. 2003 May 1;56(1):266–73.

59. Giaddui T, Cui Y, Galvin J, Yu Y, Xiao Y. Comparative dose evaluations between XVI and OBI cone beam CT systems using Gafchromic XRQA2 film and nanoDot optical stimulated luminescence dosimeters. Med Phys. 2013 Jun 1;40(6Part1):n/a-n/a.

60. Linthout N, Verellen D, Tournel K, Reynders T, Duchateau M, Storme G. Assessment of secondary patient motion induced by automated couch movement during on-line 6 dimensional repositioning in prostate cancer treatment. Radiother Oncol. 2007 May 1;83(2):168–74.

61. Bourland JD. Image-Guided Radiation Therapy. CRC Press; 2012. 258 p.

62. Systems and methods for monitoring patient motion via capacitive position sensing [Internet]. 2016 [cited 2017 Jul 31]. Available from: https://patents.google.com/patent/WO2017063084A1/en

63. Mehta VKM& R. S. Chand's Principle Of Physics -XII. S. Chand Publishing; 1601 p.

64. Wilson JS. Sensor Technology Handbook [Internet]. Amsterdam: Newnes; 2005. Available from: http://ezproxy.library.dal.ca/login?url=http://search.ebscohost.com/login.aspx?direct=true&db=nlebk&AN=117182&site=ehost-live

65. Hector LG, Schultz HL. The Dielectric Constant of Air at Radiofrequencies. Physics. 1936 Apr 1;7(4):133–6.

66. Baxter LK. Capacitive Sensors: Design and Applications. IEEE Press; 1997. 330 p.

67. Siauve N, Scorretti R, Burais N, Nicolas L, Nicolas A. Electromagnetic fields and human body: a new challenge for the electromagnetic field computation. COMPEL Int J Comput Math Electr Electron Eng. 2003;22(3):457–69.

68. Yazdi N, Ayazi F, Najafi K. Micromachined inertial sensors. Proc IEEE. 1998 Aug;86(8):1640–59.

69. Zhang Y, Howver R, Gogoi B, Yazdi N. A high-sensitive ultra-thin MEMS capacitive pressure sensor. In: 2011 16th International Solid-State Sensors, Actuators and Microsystems Conference. 2011. p. 112–5.

70. Lin JT, Jackson D, Aebersold J, Walsh KM, Naber J, Hnat W. A High Gauge Factor Capacitive Strain Sensor and its Telemetry Application in Biomechanics. In: 2008 17th Biennial University/Government/Industry Micro/Nano Symposium. 2008. p. 98–101.

71. Chu LL, Gianchandani YB. A micromachined 2D positioner with electrothermal actuation and sub-nanometer capacitive sensing. J Micromechanics Microengineering. 2003;13(2):279.

72. Lazarus N, Bedair SS, Lo CC, Fedder GK. CMOS-MEMS Capacitive Humidity Sensor. J Microelectromechanical Syst. 2010 Feb;19(1):183–91.

73. Smith J, White T, Dodge C, Paradiso J, Gershenfeld N, Allport D. Electric field sensing for graphical interfaces. IEEE Comput Graph Appl. 1998 May;18(3):54–60.

74. Togura T, Nakamura Y, Akashi K. Long-Range Human Body Sensing Modules with Electric Field Sensor [Internet]. Warrendale, PA: SAE Technical Paper; 2008 Apr [cited 2017 Aug 3]. Report No.: 2008-1–909. Available from: http://papers.sae.org/2008-01-0909/

75. Karlsson N. A capacitance sensor for safeguarding operators of industrial robots. Robotica. 1999 Jan;17(1):33–9.

76. SEMTECH. Capacitive Touch Sensing Layout Guidelines [Internet]. [cited 2017 Jul 31]. Available from: http://www.mouser.com/pdfdocs/semtech-capacitive-touch-sensing-layout-guidelines.pdf

77. Union College. Capacitance and Resistance [Internet]. [cited 2017 Aug 27]. Available from: http://minerva.union.edu/labrakes/Capacitance%20and%20Resistance.pdf

78. Feng Y, Abney TM, Okamoto RJ, Pless RB, Genin GM, Bayly PV. Relative brain displacement and deformation during constrained mild frontal head impact. J R Soc Interface. 2010 Dec 6;7(53):1677–88.

APPENDIX A COPYRIGHT PERMISSIONS

Requestor Location	Dalhousie University 6299 South St Halifax, NS B3H4R2 Canada Attn: Dalhousie University
Total	0.00 USD

This Agreement between Dalhousie University -- Ethan Avila Ruiz ("You") and Elsevier ("Elsevier") consists of your license details and the terms and conditions provided by Elsevier and Copyright Clearance Center.

License Number	4161111478383
License date	Aug 02, 2017
Licensed Content Publisher	Elsevier
Licensed Content Publication	International Journal of Radiation Oncology*Biology*Physics
Licensed Content Title	Clinical Evaluation of a Robotic 6-Degree of Freedom Treatment Couch for Frameless Radiosurgery
Licensed Content Author	Thierry Gevaert,Dirk Verellen,Benedikt Engels,Tom Depuydt,Karina Heuninckx,Koen Tournel,Michael Duchateau,Truus Reynders,Mark De Ridder
Licensed Content Date	Jan 1, 0001
Licensed Content Volume	83
Licensed Content Issue	1
Licensed Content Pages	8
Start Page	467
End Page	474
Type of Use	reuse in a thesis/dissertation
Portion	figures/tables/illustrations
Number of figures/tables/illustrations	1
Format	both print and electronic
Are you the author of this Elsevier article?	No
Will you be translating?	No
Original figure numbers	Figure 3
Title of your thesis/dissertation	A CAPACITIVE MONITORING SYSTEM FOR STEREOTACTIC RADIOSURGERY: DETECTOR DESIGN
Expected completion date	Aug 2017
Estimated size (number of pages)	80
Requestor Location	Dalhousie University 6299 South St

80

Halifax, NS B3H4R2
Canada
Attn: Dalhousie University

Total   0.00 USD

This Agreement between Dalhousie University -- Ethan Avila Ruiz ("You") and Elsevier ("Elsevier") consists of your license details and the terms and conditions provided by Elsevier and Copyright Clearance Center.

License Number	4160000514845
License date	Aug 01, 2017
Licensed Content Publisher	Elsevier
Licensed Content Publication	International Journal of Radiation Oncology*Biology*Physics
Licensed Content Title	Is mask-based stereotactic head-and-neck fixation as precise as stereotactic head fixation for precision radiotherapy?
Licensed Content Author	Dietmar Georg,Joachim Bogner,Karin Dieckmann,Richard Pötter
Licensed Content Date	Nov 15, 2006
Licensed Content Volume	66
Licensed Content Issue	4
Licensed Content Pages	6
Start Page	S61
End Page	S66
Type of Use	reuse in a thesis/dissertation
Portion	figures/tables/illustrations
Number of figures/tables/illustrations	1
Format	both print and electronic
Are you the author of this Elsevier article?	No
Will you be translating?	No
Original figure numbers	Figure 3
Title of your thesis/dissertation	A CAPACITIVE MONITORING SYSTEM FOR STEREOTACTIC RADIOSURGERY: DETECTOR DESIGN
Expected completion date	Aug 2017
Estimated size (number of pages)	80
Requestor Location	Dalhousie University 6299 South St

82

Halifax, NS B3H4R2
Canada
Attn: Dalhousie University

Total   0.00 USD

This Agreement between Dalhousie University -- Ethan Avila Ruiz ("You") and John Wiley and Sons ("John Wiley and Sons") consists of your license details and the terms and conditions provided by John Wiley and Sons and Copyright Clearance Center.

License Number	4159660687513
License date	Jul 31, 2017
Licensed Content Publisher	John Wiley and Sons
Licensed Content Publication	Medical Physics
Licensed Content Title	Characterization of a real-time surface image-guided stereotactic positioning system
Licensed Content Author	Jean L. Peng,Darren Kahler,Jonathan G. Li,Sanjiv Samant,Guanghua Yan,Robert Amdur,Chihray Liu
Licensed Content Date	Sep 28, 2010
Licensed Content Pages	13
Type of use	Dissertation/Thesis
Requestor type	University/Academic
Format	Print and electronic
Portion	Figure/table
Number of figures/tables	3
Original Wiley figure/table number(s)	Figure 8, Figure 9
Will you be translating?	No
Title of your thesis / dissertation	A CAPACITIVE MONITORING SYSTEM FOR STEREOTACTIC RADIOSURGERY: DETECTOR DESIGN
Expected completion date	Aug 2017
Expected size (number of pages)	80
Requestor Location	Dalhousie University 6299 South St Halifax, NS B3H4R2 Canada Attn: Dalhousie University

84

Publisher Tax ID	EU826007151
Billing Type	Invoice
Billing Address	Dalhousie University 6299 South St Halifax, NS B3H4R2 Canada Attn: Dalhousie University
Total	0.00 USD